Wavenumber-frequency analysis of single-layer shallow-water beta-plane quasi-geostrophic turbulence

A. J. Morten, B. K. Arbic, and G. R. Flierl

Citation: Physics of Fluids **29**, 106602 (2017); doi: 10.1063/1.5003846
View online: http://dx.doi.org/10.1063/1.5003846
View Table of Contents: http://aip.scitation.org/toc/phf/29/10
Published by the American Institute of Physics

PHYSICS OF FLUIDS **29**, 106602 (2017)

Wavenumber-frequency analysis of single-layer shallow-water beta-plane quasi-geostrophic turbulence

A. J. Morten,[1,a)] B. K. Arbic,[2] and G. R. Flierl[3]
[1] *Department of Physics, University of Michigan, Ann Arbor, Michigan 48109, USA*
[2] *Department of Earth and Environmental Sciences, University of Michigan, Ann Arbor, Michigan 48109, USA*
[3] *Department of Earth, Atmospheric, and Planetary Sciences, Massachusetts Institute of Technology, Cambridge, Massachusetts 02139, USA*

(Received 10 February 2017; accepted 7 September 2017; published online 10 October 2017)

We numerically investigate single-layer shallow-water beta-plane quasi-geostrophic turbulence in a doubly periodic domain with emphasis on wavenumber-frequency spectra. We conduct a broad parameter sweep, varying the deformation radius (L_d), the narrow-band forcing wavenumber (k_f), and the meridional gradient of the Coriolis parameter (β). Out of 54 simulations we present ten in detail spanning slowly propagating vortices to strong jets. We define a nondimensional parameter γ_β in terms of β, L_d, and the energy injection rate. The moderately low γ_β case is characterized by westward propagating coherent vortices and zonal wavenumber-frequency spectra dominated by a nondispersive line (NDL) corresponding to uniform propagation at or near the long-wave Rossby speed. The moderately high γ_β case is characterized by jets, and the NDL persists even when there are no coherent vortices. The jets have large meridional excursions (meanders) that propagate westward nearly uniformly at a speed slower than the long-wave Rossby speed. Also at moderately high γ_β, a second dispersion relation appears, roughly corresponding to linear waves on a zonal potential vorticity (PV) staircase. At very high γ_β, during the slow evolution to a PV staircase, the structure of the linear waves is altered by the small perturbations to a constant potential vorticity gradient. A simple model treating the small perturbation as a sinusoid accurately predicts the meridional wavenumber-frequency spectra in the very high γ_β simulations. *Published by AIP Publishing.* https://doi.org/10.1063/1.5003846

I. INTRODUCTION

Satellite altimetric measurements of sea surface height, with relatively high resolution in both space and time, have made it possible to conduct systematic studies of the ocean in the wavenumber-frequency domain.[1–4] To aid in interpreting the oceanic spectra, we examine the wavenumber-frequency spectra produced by numerical simulations of a simple model for large-scale oceanic dynamics. For this purpose, we numerically investigate the single-layer shallow-water beta-plane quasi-geostrophic equation (also known as the 1.5-layer model) over a wide range of parameters, providing a comprehensive review of the wavenumber-frequency spectra that characterize the various flow regimes. While the motivation arises from oceanography, we consider a range of parameters relevant to Earth's oceans and atmosphere, as well as the atmospheres of gas giants.

The 1.5-layer model defined below by Eq. (1) is one of the simplest models for deformation-scale oceanic and atmospheric dynamics. The key parameters are the deformation radius L_d (or its inverse, $k_d := 1/L_d$), the meridional gradient β of the Coriolis parameter, and the narrow-band forcing wavenumber k_f. The case where k_d and β are both nonzero has not been investigated via direct numerical simulation nearly as often as the cases where either k_d or β (or both) is zero.

When both k_d and β are zero, the system reduces to the two-dimensional Navier-Stokes equations with external forcing and modified dissipation. Whereas in three dimensions, the kinetic energy famously cascades from the forcing scale to smaller scales,[5–9] in two dimensions, a dual cascade forms. In the dual cascade picture, kinetic energy cascades from the forcing scale to larger scales, while enstrophy cascades from the forcing scale to smaller scales.[10–13] The inverse cascade of energy plays an important role in the phenomenology of the more general quasi-two-dimensional system with nonzero k_d and β.

The case of infinite deformation radius on the beta plane ($k_d = 0$, $\beta \neq 0$) has been studied extensively. Rhines[14] predicted that the inverse cascade of kinetic energy is nearly arrested near what is now called the Rhines wavenumber, at which the beta term in the governing equation reaches the same magnitude as the nonlinear advection term. Near the Rhines wavenumber, the influence of the beta term leads to anisotropic flow, which can take the form of zonal jets. Sukoriansky, Dikovskaya, and Galperin[15] clarified the interpretation of the Rhines wavenumber, arguing that the Rhines scale (the inverse of the Rhines wavenumber) is not associated with the arrest of the inverse cascade because the cascade continues anisotropically to larger scales until frictional effects are felt. Relatedly, Vallis and Maltrud[16] derived a transition wavenumber, which serves the same purpose as the Rhines wavenumber but can be calculated in terms of the energy injection rate.

The case of finite deformation radius on the f-plane ($k_d \neq 0$, $\beta = 0$) is equivalent to the Charney-Hasegawa-Mima

---

[a)] amorten@umich.edu

equation,[17,18] which models drift-wave turbulence in magnetically confined plasmas (e.g., tokamaks). The inverse cascade of kinetic energy generalizes to an inverse cascade of total energy, which is the sum of kinetic and (available) potential energy. The finite deformation radius shields the kinetic energy cascade, allowing only potential energy to cascade to larger scales. Theoretical studies sometimes take the limit $k_d \to \infty$, in which case potential and kinetic energy actually cascade in opposite directions. Here we are interested in values of k_d that are finite but not too large.

We investigate the more general case where both $k_d \neq 0$ and $\beta \neq 0$. Kukharkin and Orszag[19] found that switching k_d to a nonzero value destabilizes jets that form when k_d is zero. Consistent with that finding, Okuno and Masuda[20] derived a modified Rhines number for nonzero k_d and showed that when k_d is sufficiently large, the anisotropization of the flow is suppressed because the beta term cannot dominate the nonlinear term. Smith[21] conducted a systematic numerical investigation, focusing on the parameter requirements for anisotropy and the production of jets, thereby deriving a modified transition wavenumber that generalizes that of Vallis and Maltrud.[16] Here we consider both the modified Rhines wavenumber and modified transition wavenumber described above, and we elucidate their relationship.

The main contribution of our research is the systematic investigation of wavenumber-frequency spectra for the general case with $k_d \neq 0$ and $\beta \neq 0$. Previously, Zhang and Afanasyev[22] conducted an experimental study of barotropic and baroclinic turbulent flows generated in a rotating tank with a topographic beta effect. They observed the creation of jets and found evidence of linear Rossby waves in wavenumber-frequency spectra at low wavenumbers. Suhas and Sukhatme[23] conducted a numerical investigation with emphasis on wavenumber-frequency spectra, also finding that much of the kinetic energy at large scales lies along the Rossby dispersion curve when there are jets. We conduct a broader parameter sweep at higher resolution and show that the spectra at smaller scales indicate phenomena other than Rossby waves.

The motivation for our study is partly based on a desire to understand the nondispersive line (NDL) observed in zonal wavenumber-frequency spectra for several regions of the ocean.[2] The observed NDL's slope is somewhat larger than that of the long baroclinic Rossby wave; a similar increase is found in reducing a two-layer model to motions only in the upper layer (as in our 1.5-layer model). The deep velocities may be smaller because topography destroys the coherence between the upper and lower layers.[24] This is related to the finding that in two-layer models, mid-ocean eddies are best modeled by flows with a moderate level of damping.[25] Therefore the 1.5-layer system seems to be a reasonable model for investigating the NDL.

The slope and narrowness of the observed NDL imply that moderately coherent structures propagate westward at a roughly uniform speed. Early, Samelson, and Chelton[26] investigated the NDL in numerical simulations seeded with Gaussian-profile vortices similar to oceanic eddies. The vortices propagated westward somewhat coherently, with occasional merging, distortion by interaction, and diversion from uniform westward propagation. The resulting spectra were dominated by a NDL. In simulations of a two-layer model, a NDL also appears when there are high-amplitude westward propagating vortices.[27,28] Thus, a natural hypothesis is that the observed NDL is due primarily to westward propagating coherent vortices. However, we will show via numerical simulation that a NDL can dominate spectra even when there are no coherent vortices because jet meanders also tend to propagate uniformly westward for a wide range of parameters. Caution is therefore warranted when attributing the NDL to specific spatial characteristics of the flow.

The NDL is not the only spectral feature that appears in wavenumber-frequency spectra for simulations of Eq. (1). As will be seen, at least two other dispersion relations often arise in simulations. The purpose of this paper is to review and explain the various wavenumber-frequency spectra that arise for a wide set of parameters. We also identify the corresponding flow characteristics and consider the nondimensional parameters that determine the various flow regimes.

The remainder of this paper is organized as follows. In Sec. II, we describe the numerical simulations and determine the relevant nondimensional parameters. In Secs. III–V, we investigate the flow characteristics and wavenumber-frequency spectra for three different flow regimes, using linear wave theory to explain some of the spectral features. In Sec. VI, we summarize the findings for all simulations.

II. NUMERICAL SETUP

We numerically simulate forced-dissipated single-layer shallow-water beta-plane quasi-geostrophic turbulence over a square domain with doubly periodic boundary conditions (with spatial period $L = 2\pi$ in both the x- and y-direction). The equation of motion is

$$\partial_t \left(\nabla^2 - k_d^2\right)\psi + J\left(\psi, \nabla^2\psi + \beta y\right) = \left(\nu_{-2}\nabla^{-2} + \nu_6\nabla^6\right)\nabla^2\psi + \mathcal{F}. \tag{1}$$

The stream function $\psi(x, y, t)$ is related to potential vorticity (PV) q by the definition

$$q := \nabla^2\psi - k_d^2\psi + \beta y, \tag{2}$$

where k_d is related to the deformation radius $L_d = 1/k_d$ and β is the meridional gradient of the Coriolis parameter. The Jacobian is defined as $J(A, B) := (\partial_x A)(\partial_y B) - (\partial_y A)(\partial_x B)$. For dissipation, we employ low-order hypoviscosity (∇^{-2}) with coefficient ν_{-2} and hyperviscosity (∇^6) with coefficient ν_6 applied to the relative vorticity. The hypoviscosity is equivalent to a thermal damping and is used because it allows a wider inertial range than would a linear drag.

The forcing term $\mathcal{F}$ is statistically isotropic in space, narrow-band in wavenumber, and stochastic (effectively white noise) in time. The amplitude of the forcing is normalized so that the spatial average of $\mathcal{F}^2$ is one. The forcing is defined in detail in Appendix D.

We simulate Eq. (1) using a pseudo-spectral method with spatial resolution 1024^2. The time-stepping is performed with a third-order Adams–Bashforth method for ψ and Euler's method (with a smaller time increment, constant across all runs) for $\mathcal{F}$. The pseudo-spectral method is based on the spatial Fourier transform of Eq. (1),

$$\partial_t\left(\kappa^2+k_d^2\right)\widetilde{\psi}-\widetilde{J\left(\psi,\nabla^2\psi+\beta y\right)}=-\left(\nu_{-2}\kappa^{-2}+\nu_6\kappa^6\right)\kappa^2\widetilde{\psi}-\widetilde{\mathcal{F}}. \tag{3}$$

By definition k is the zonal wavenumber (in the x, or east-west, direction), l is the meridional wavenumber (in the y, or north-south, direction), and $\kappa := (k^2 + l^2)^{1/2}$ is the isotropic wavenumber.

The dissipation coefficients vary dynamically during spin-up but are set to fixed values after statistical equilibrium is reached. The coefficient of hypoviscosity is chosen such that on average one tenth of the total potential energy is in spatial modes $\kappa \leq 3$, ensuring that potential energy does not saturate at the domain scale. The coefficient of hyperviscosity is chosen such that on average 1×10^{-10} of the total enstrophy is in spatial modes $\kappa \geq 2k_{Ny}/3 \approx 342$, where k_{Ny} is the Nyquist wavenumber. This choice of hyperviscosity coefficient ensures a nearly complete de-aliasing of the nonlinear term via the 2/3 rule.[29,30]

Statistical steadiness was determined by inspecting time series of various scalar quantities, including total kinetic energy, total enstrophy, k_{Rh}, k_β, and k_{PE} (the latter three quantities will be defined shortly). Because potential energy cascades to large scales relatively slowly in simulations with jets, the most useful quantities to track were the total potential energy and the fraction of potential energy in modes $\kappa \leq 3$. Whenever the latter quantity stabilized at 10% (due to dynamic hypoviscosity), potential energy had reached the largest scales available, and all other quantities appeared to be statistically steady.

In order to construct a parameter sweep for Eq. (3), we must specify the relevant nondimensional parameters. We do so by determining the important length scales (or corresponding wavenumbers) and constructing their ratios. Two obvious candidates are the deformation wavenumber k_d and the narrow-band forcing wavenumber k_f. In forced-dissipated simulations, two more length scales are set by the large-scale dissipation of energy and the small-scale dissipation of enstrophy.

Because we are using thermal damping for the large-scale dissipation, the dissipation of total energy in wavenumber space is proportional to the potential energy spectrum. Therefore, we define the large-scale dissipation wavenumber to be the wavenumber centroid of potential energy

$$k_{PE} := \frac{\iint dk\, dl\ \kappa\left|\widetilde{\psi}(k,l,t)\right|^2}{\iint dk\, dl\ \left|\widetilde{\psi}(k,l,t)\right|^2}. \tag{4}$$

The large-scale dissipation wavenumber is a key parameter in the infinite deformation radius case because the energy cascade is not arrested at the Rhines scale.[15,31,32] Similarly, when the deformation radius is finite, the total energy is likely not arrested at the modified Rhines scale but continues to cascade anisotropically to larger scales until removed by large-scale dissipation. We therefore include k_{PE} in our parameterization.

The small-scale dissipation wavenumber k_{diss}, where the potential enstrophy cascade is halted by hyperviscosity, could also be relevant, but we simply make it as large as possible and thereafter ignore it. The ratio k_{diss}/k_f is sometimes not very large, however, leaving little room for an enstrophy cascade. Whatever effect k_{diss}/k_f has on the dynamics is left as an open question.

By combining k_d, k_f, and k_{PE} we obtain two nondimensional parameters. Within the inverse cascade of total energy, potential energy dominates kinetic energy in the region $k_{PE} < \kappa < k_d$, so the nondimensional parameter

$$\gamma_d := \frac{k_d}{k_{PE}} \tag{5}$$

measures the width of the potential energy cascade. Similarly, kinetic energy dominates the inverse cascade in the region $k_d < \kappa < k_f$, so the nondimensional parameter

$$\gamma_f := \frac{k_f}{k_d} \tag{6}$$

measures the width of the kinetic energy cascade. The product $\gamma_d\gamma_f = k_f/k_{PE}$ measures the width of the full inverse cascade of total energy.

To specify the parameter sweep we must define an additional length scale that takes into account the strength of the beta term. There are multiple possibilities, depending on whether we use the Rhines wavenumber or the transition wavenumber, as mentioned in the Introduction. The Rhines wavenumber[14] is

$$k_{Rh} := \sqrt{\beta/2U_{rms}}, \tag{7}$$

where U_{rms} is the root-mean-square velocity of the fluid. The transition wavenumber[16] is

$$k_\beta := \left(\beta^3/\mathcal{C}^{3/2}\epsilon\right)^{1/5}, \tag{8}$$

where $\mathcal{C}$ is the Kolmogorov constant and ϵ is the mean rate of upscale energy transfer (i.e., the rate of energy injection by the forcing minus the energy dissipation rate at small scales). Both k_{Rh} and k_β are predictions for the wavenumber at which anisotropy will develop when $k_d = 0$.

Using k_{Rh} and k_β we define two nondimensional parameters,

$$\gamma_{Rh} := \frac{k_{Rh}}{k_d} \tag{9}$$

and

$$\gamma_\beta := \frac{k_\beta}{k_d}. \tag{10}$$

Either can be selected as the final independent nondimensional parameter. Note that both γ_{Rh} and γ_β must be determined *post priori*, since neither U_{rms} nor ϵ can be determined *a priori* (given our choice of stochastic forcing).

Both γ_{Rh} and γ_β compare k_d to the predicted wavenumber at which anisotropy would develop if k_d were zero. Alternatively, both γ_{Rh} and γ_β can be thought of as the unique (up to an arbitrary power and multiplicative constant) dimensionless monomial combination of β, k_d, and either U_{rms} or ϵ. As detailed below, γ_{Rh} and γ_β can also be used to predict whether and at which wavenumber anisotropy will develop for the general case $k_d \neq 0$.

The derivation of the Rhines wavenumber k_{Rh} can be modified to include the effect of a finite deformation radius, as shown in the work of Okuno and Masuda.[20] The result is the modified Rhines wavenumber,

$$k'_{Rh} := \sqrt{k_{Rh}^2 - k_d^2} \tag{11}$$

$$= k_d\sqrt{\gamma_{Rh}^2 - 1}, \tag{12}$$

the predicted wavenumber at which anisotropy develops when $k_d \neq 0$. The modified Rhines wavenumber is only defined when $\gamma_{Rh} \geq 1$ or, equivalently, when $k_{Rh} \geq k_d$. Thus, anisotropy will not develop if k_d is too large. This inhibition of the beta effect by a finite deformation radius (and hence inhibition of jets) has been useful in explaining the positions of stormy regions on Jupiter[33] and Saturn.[34]

While Eq. (12) predicts that anisotropy will develop only when $\gamma_{Rh} > 1$, the derivation is actually based on an order of magnitude estimate that leaves out a possible $O(1)$ factor. The arbitrary factor multiplies γ_{Rh} in Eq. (12), so the theory actually predicts that there is a $O(1)$ critical value $\gamma_{Rh,crit}$ that separates isotropy from anisotropy. We later report the value of $\gamma_{Rh,crit}$ based on our simulations.

We can also derive a modified transition wavenumber that generalizes k_β for flows with $k_d \neq 0$. The modified transition wavenumber k'_β is derived by equating the Rossby wave frequency with the inverse of the theoretical eddy turnover time,

$$\tau^{-1} = \mathcal{C}^{1/2}\epsilon^{1/3}\kappa^{2/3}. \tag{13}$$

The difference with the derivation of k_β is that when the deformation radius is finite, the Rossby dispersion relation becomes

$$\omega = \omega_R(k,l) := \frac{-\beta k}{k^2 + l^2 + k_d^2}. \tag{14}$$

The result is the modified transition wavenumber k'_β defined implicitly by

$$k'_\beta := \text{largest } \kappa \text{ that solves } \quad \gamma_\beta^{5/3}(\kappa/k_d)^{1/3} = (\kappa/k_d)^2 + 1, \tag{15}$$

which is equivalent to the result derived by Smith.[21]

Anisotropy develops only when Eq. (15) has a solution, which happens only when $\gamma_\beta > 1.3$. However, the derivation of k'_β also leaves out an $O(1)$ multiplicative factor when equating the inverse eddy turnover time with the Rossby wave frequency. Thus, the critical value $\gamma_{\beta,crit}$ that separates isotropy from anisotropy should be near, but not necessarily precisely at, $\gamma_\beta = 1.3$. In Sec. VI, we report the value of $\gamma_{\beta,crit}$ based on our simulations.

Smith[21] defines the nondimensional parameter $\tilde{\beta} := \beta(\epsilon k_d^5)^{-1/3}$, which is related to γ_β by

$$\tilde{\beta} = \mathcal{C}^{1/2}\gamma_\beta^{5/3}. \tag{16}$$

The parameters $\tilde{\beta}$ and γ_β are interchangeable, differing only by a power and a multiplicative constant, but we prefer γ_β due to its interpretation as the ratio of k_β to k_d. The predicted threshold for anisotropy at $\gamma_\beta = 1.3$ corresponds to $\tilde{\beta} = 3.9$. To facilitate a comparison with Smith,[21] we report both γ_β and $\tilde{\beta}$ in Table I.

In summary, each simulation is characterized by three nondimensional parameters: γ_d, γ_f, and either γ_β or γ_{Rh}. The parameters γ_d and γ_f determine the widths of the potential and kinetic energy cascades, respectively. The parameters γ_β and γ_{Rh} determine the relative importance of the beta term, and in theory they both determine the transition to anisotropy or jets.

We conduct a parameter sweep over the dimensional parameters k_d, k_f, and β, from which we derive the nondimensional parameters. We choose three values of $\gamma_d = k_d/k_{PE}$ that span the observed values in the North Atlantic calculated by Eden.[35] The wavenumber k_{PE} is a time-varying quantity, and for most equilibrated simulations, the time-averaged value is roughly $k_{PE} \approx 5$. Thus, by setting $k_d \in \{6, 15, 30\}$, we obtain the approximate values $\gamma_d \in \{1.2, 3, 6\}$. The middle value is the most common in the North Atlantic and the outer values lie near the extrema of the observations. For the forcing wavenumber (which determines γ_f), we choose $k_f \in \{6, 15, 30, 90\}$ subject to the constraint $k_f \geq k_d$. That is, we force at scales roughly equal to and smaller than the deformation radius. The resulting possible values of γ_f span the range $1 \leq \gamma_f \leq 15$. Because both γ_{Rh} and γ_β are determined *post priori*, in order to determine them we simply vary β over a wide range and then report the resulting nondimensional parameters. We conduct simulations for all $\beta \in \{0, 0.1, 1, 10, 100, 1000\}$, which yield a wide range of flow regimes.

Altogether we simulate 54 different combinations of (k_d, k_f, β), too many to present in detail. Instead we focus on

TABLE I. Dimensional and nondimensional parameters for simulations 1–10. Also indicated are the presence of vortices (vort's), jets, and the three dispersion relations discussed in the text, including the nondispersive line (NDL). The acronym LWDR refers to the linear wave dispersion relation derived in Sec. IV, while PR refers to the periodically extended Rossby dispersion relation derived in Sec. V. Question marks indicate that the spectral feature is barely noticeable. We do not provide hypoviscosity coefficients ν_{-2} for simulations 8–10 because those three simulations are still in the spin-up phase, as explained in Sec. V.

Run	k_d	k_f	β	γ_d	γ_f	γ_{Rh}	γ_β	$\tilde{\beta}$	ν_{-2}	ν_6	Spatial and spectral features			
1	15	90	1	3.1	6.0	0.17	0.4	0.59	0.04	1.3×10^{-28}	vort's		NDL	
2	15	30	10	3.2	2.0	0.41	1.1	2.8	0.1	7.7×10^{-29}	vort's		NDL	
3	6	6	10	1.4	1.0	0.75	1.2	3.1	1.4	6.0×10^{-29}	vort's		NDL	
4	15	90	10	3.3	6.0	0.54	1.9	6.9	0.02	1.3×10^{-28}	vort's	jets	NDL	LWDR
5	6	90	10	1.4	15.	0.92	3.4	19	0.015	1.3×10^{-28}	vort's	jets	NDL	LWDR
6	6	6	100	1.3	1.0	0.91	4.1	26	0.06	3.9×10^{-29}		jets	NDL	
7	15	90	100	2.4	6.0	0.77	7.3	68	0.01	6.5×10^{-29}		jets	NDL	LWDR
8	30	90	1000	1.4	3.0	1.6	15	210	…	9.7×10^{-29}		jets	NDL?	PR
9	15	30	1000	1.3	2.0	2.3	20	370	…	7.0×10^{-29}		jets	NDL?	PR
10	15	90	1000	1.3	6.0	3.2	30	700	…	1.1×10^{-28}		jets		PR?

ten representative examples and then summarize the remaining simulations. Table I lists the dimensional and nondimensional parameters for these ten simulations.

We identify four flow regimes, determined by the ratio of γ_β to $\gamma_{\beta,crit}$ (the threshold that separates isotropy from anisotropy). When $\gamma_\beta \ll \gamma_{\beta,crit}$, the flows are nearly indistinguishable from the $\beta = 0$ case, in which we are not interested. In Sec. III, we consider the case $\gamma_\beta \lesssim \gamma_{\beta,crit}$, distinguished by westward propagating vortices and the absence of jets. In Sec. IV, we investigate the case $\gamma_\beta \gtrsim \gamma_{\beta,crit}$, distinguished by meandering jets approximating a potential vorticity (PV) staircase and nearly uniform westward propagation. In Sec. V, we consider the final case $\gamma_\beta \gg \gamma_{\beta,crit}$, which approaches statistical equilibrium very slowly and is distinguished by jets and linear Rossby-like waves during spin-up and a PV staircase once equilibrium is reached.

It is important to clarify what we mean by a "jet." In this paper, a jet is a region of large potential vorticity gradient ($dq/dy > 1.5\beta$) that spans the domain zonally. The jets are easily identifiable in snapshots of $q - \beta y$ and are similar to the jets found on giant gas planets. An alternative definition for "jet" would be the presence of zonal bands in the time-averaged velocity field. Like striations in the ocean, such jets might not be apparent without significant time-averaging. We do not consider such time-averaged jets here.

Throughout this paper we diagnose various forms of wavenumber-frequency spectra, namely, the full wavenumber-frequency kinetic energy spectrum

$$\mathcal{K}(k,l,\omega) := \tfrac{1}{2}\kappa^2\left|\widehat{\widetilde{\psi}}(k,l,\omega)\right|^2, \tag{17}$$

the zonal wavenumber-frequency kinetic energy spectrum

$$\mathcal{K}(k,\omega) := \sum_l \mathcal{K}(k,l,\omega), \tag{18}$$

and the meridional wavenumber-frequency kinetic energy spectrum

$$\mathcal{K}(l,\omega) := \sum_k \mathcal{K}(k,l,\omega), \tag{19}$$

where ω denotes frequency. For notational convenience, the symbol $\mathcal{K}$ is used for each of the three spectra, even though they are different functions. The meaning in each case is made clear by the arguments. In Eq. (17), the "tilde" operator is the spatial discrete Fourier transform (DFT) while the "hat" operator is the temporal DFT using a Tukey window. Additional theory is developed as needed throughout the remainder of this paper.

III. MODERATELY LOW $\gamma_\beta \lesssim \gamma_{\beta,crit}$ (WESTWARD PROPAGATING VORTICES)

In this section, we consider simulations with γ_β below but near the threshold for jet formation. In this case, it is well known that westward propagating coherent vortices form and that their propagation speed roughly equals the long-wave Rossby speed,

$$c_R := -\beta L_d^2 = -\beta/k_d^2. \tag{20}$$

Because quasi-isotropic, westward-propagating vortices are a dominant feature of the ocean,[26,36] the simulations reported in this section are the most likely to be oceanographically relevant.

We present three representative cases (simulations 1–3) with defining parameters given in Table I. The respective values for γ_β are (0.4, 1.1, 1.2) and for γ_{Rh} are (0.17, 0.41, 0.75). Both k_f and γ_f vary significantly among this set of simulations, with $(k_f, \gamma_f) = (90, 6)$, (30, 2), and (6, 1) for simulations 1–3, respectively.

Snapshots of $q - \beta y = \nabla^2\psi - k_d^2\psi$, as well as meridional profiles of the full potential vorticity q, for simulations 1–3 are shown in Fig. 1. All three flows are dominated by quasi-isotropic, westward propagating coherent vortices.[37] Coherent vortex size appears to be constrained by the forcing scale rather than by the deformation radius. This contrasts with multi-layer

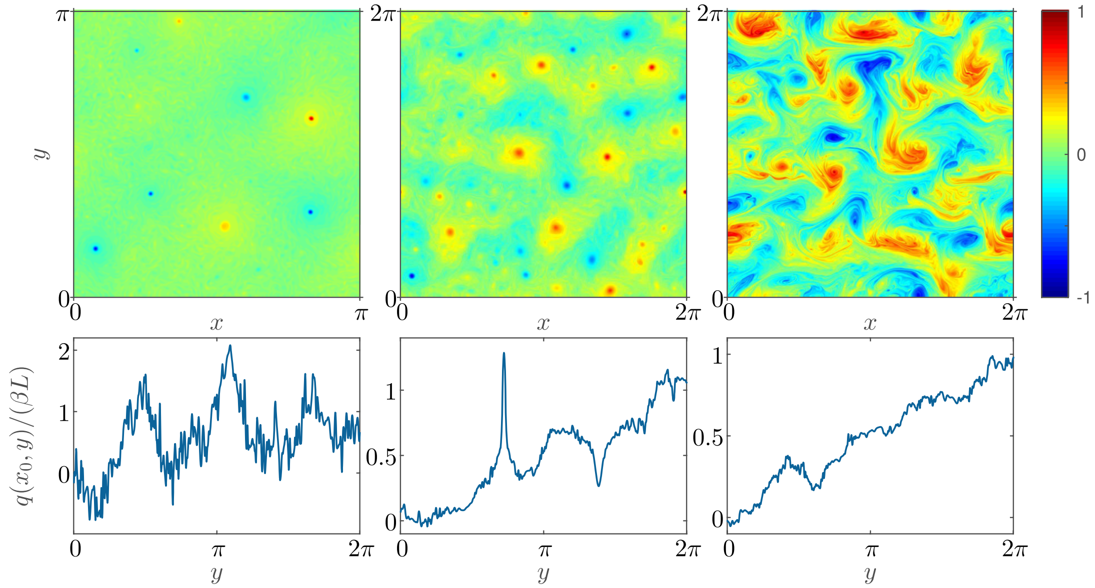

FIG. 1. For simulations 1–3 (left-to-right), snapshots of $q - \beta y$ (top row) and corresponding meridional profiles of q (bottom row). In the snapshots, $q - \beta y$ is normalized by the maximum value of $|q - \beta y|$. The snapshot for simulation 1 is magnified to show the vortices.

models in which vortex size may be set by baroclinic instability (and therefore by k_d) rather than by an imposed forcing scale. Thus, in terms of coherent vortex size, the simulations with $\gamma_f \approx 1$ may better mimic flows with baroclinic instability than when $\gamma_f \gg 1$. The meridional profiles of q in Fig. 1 show no evidence of a potential vorticity staircase, in contrast with the meridional profiles in Sec. IV.

The zonal wavenumber-frequency spectra $\mathcal{K}(k,\omega)$ for simulations 1–3 are shown in Fig. 2 (top row). In theory, uniform zonal translation at speed c of perfectly coherent vortices would result in $k\omega$-spectra that lie exactly along the nondispersive line $\omega = ck$ (in the limit of an infinite duration window). In practice, however, because the vortices neither propagate perfectly uniformly nor maintain perfect coherence, the $k\omega$-spectra will approximate a NDL with spread in the ω-direction. Indeed, the $k\omega$-spectra in all three simulations roughly follow a NDL with speed $c \approx c_R$. In simulation 1, there are additional features resembling dual peaks in the $k\omega$-spectrum; these peaks nearly match the $k\omega$-spectra of simulations with $\beta = 0$ (not shown here). In simulations 2 and 3, there appear vertical (i.e., constant k) bands of energy that simply correspond to energy build-up at the forcing wavenumber k_f.

As shown in Fig. 2, the $l\omega$-spectrum for each simulation takes the form of an annulus centered at the origin, with locally minimal energy at $l = \omega = 0$ and maximal energy at $l \approx 5$ when $\omega = 0$. Because the flow is nearly isotropic, the kl-spectrum (not shown) is roughly radially symmetric about the origin, and because we employ large scale dissipation, the kl-spectrum has a local minimum at the origin and a local maximum at $\kappa \approx k_{PE}$. The annular kl-spectrum implies an annular $l\omega$-spectrum via the NDL dispersion relation $\omega = c_R k$.

The width of the NDL is important in determining the form of the $l\omega$-spectrum. If the dispersion relation $\omega = c_R k$ were exact, then only certain discrete values of ω would appear in the $l\omega$-spectra because k is discrete. This would lead to evenly spaced horizontal stripes at constant ω in the $l\omega$-spectra. Moreover, because k takes on integer values, the stripe spacing would equal c_R. In practice, the NDL has spread in the ω-direction, which leads to spread within each stripe. For the simulations in this section, the spread is sufficiently wide (relative to c_R) so that no horizontal bands are seen the $l\omega$-spectra. In Sec. IV, horizontal bands will appear in $l\omega$-spectra for simulations with larger γ_β, which tend to have larger c_R.

IV. MODERATELY HIGH $\gamma_\beta \gtrsim \gamma_{\beta,crit}$ (PV STAIRCASES)

We now consider simulations with γ_β above but near the threshold for jet formation. These flows are anisotropic and exhibit jets with meridional profiles that may be approximated by a PV staircase. We present four representative cases (simulations 4–7), selected to show a variety of spatial flow characteristics. The respective values for γ_β are (1.9, 3.4, 4.1, 7.3) and for γ_{Rh} are (0.54, 0.92, 0.91, 0.77). The parameters γ_d and γ_f also vary substantially, as shown in Table I.

Although simulation 4 has a lower value of γ_{Rh} than simulation 3, the former exhibits jets whereas the latter is relatively isotropic. This suggests that γ_{Rh} alone does not determine the transition to jets. The parameter γ_β does a better job in this case, as it increases from 1.2 to 1.9 between simulations 3 and 4.

Snapshots of $q - \beta y$ and meridional profiles of q for simulations 4–7 are shown in Fig. 3. While all four simulations have jets, only simulations 4 and 5 exhibit coherent vortices. The jets have significant meridional excursions, typically on the same order as the jet spacing. The meridional profiles are approximately PV staircases, meaning that regions of nearly constant potential vorticity are separated by regions of large PV gradient. In most cases, the regions of large PV gradient are relatively narrow. However, simulation 6 has relatively wide regions of large PV gradient, likely because the forcing scale is as large as the jet spacing (and is also roughly the same size as the deformation radius).

The $k\omega$-spectra for simulations 4 and 5 in Fig. 4 and for simulations 6 and 7 in Fig. 5 have several interesting features.

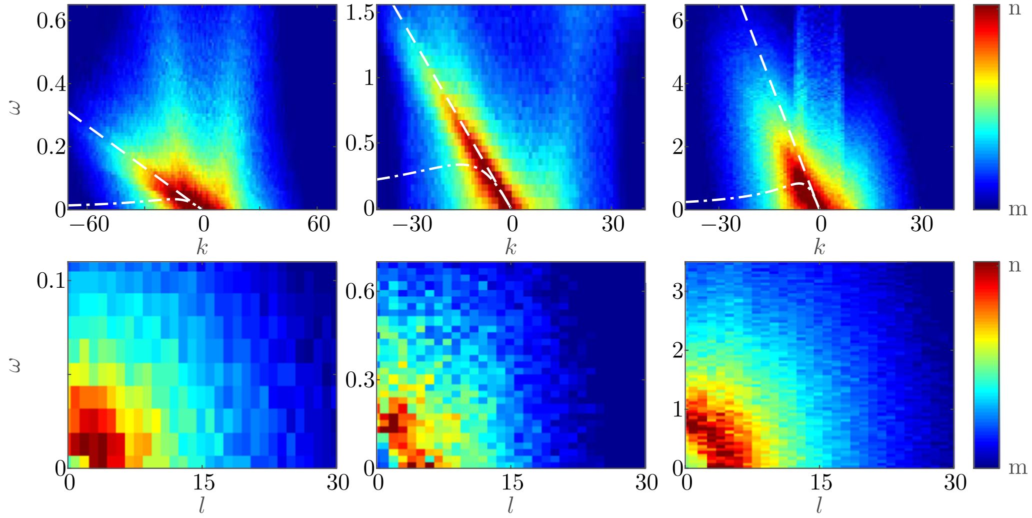

FIG. 2. For simulations 1–3 (left-to-right), the zonal wavenumber-frequency spectra $\log_{10}[\mathcal{K}(k,\omega)/\mathcal{K}_0]$ (top row) and the meridional wavenumber-frequency spectra $\log_{10}[\mathcal{K}(l,\omega)/\mathcal{K}_0]$ (bottom row). The dashed line has constant slope equal to the long-wave Rossby speed, while the dashed-dotted curve is the ($l = 0$) Rossby dispersion relation. The spectra-dependent normalization constants $\mathcal{K}_0$ are the maximum values of the corresponding spectra. The color bar scales are (m, n) = (−4.5, −2), (−4.5, −2), and (−5.5, −2) for the top row and (−3, −0.5), (−3.5, −1), and (−5, −1) for the bottom row (left-to-right).

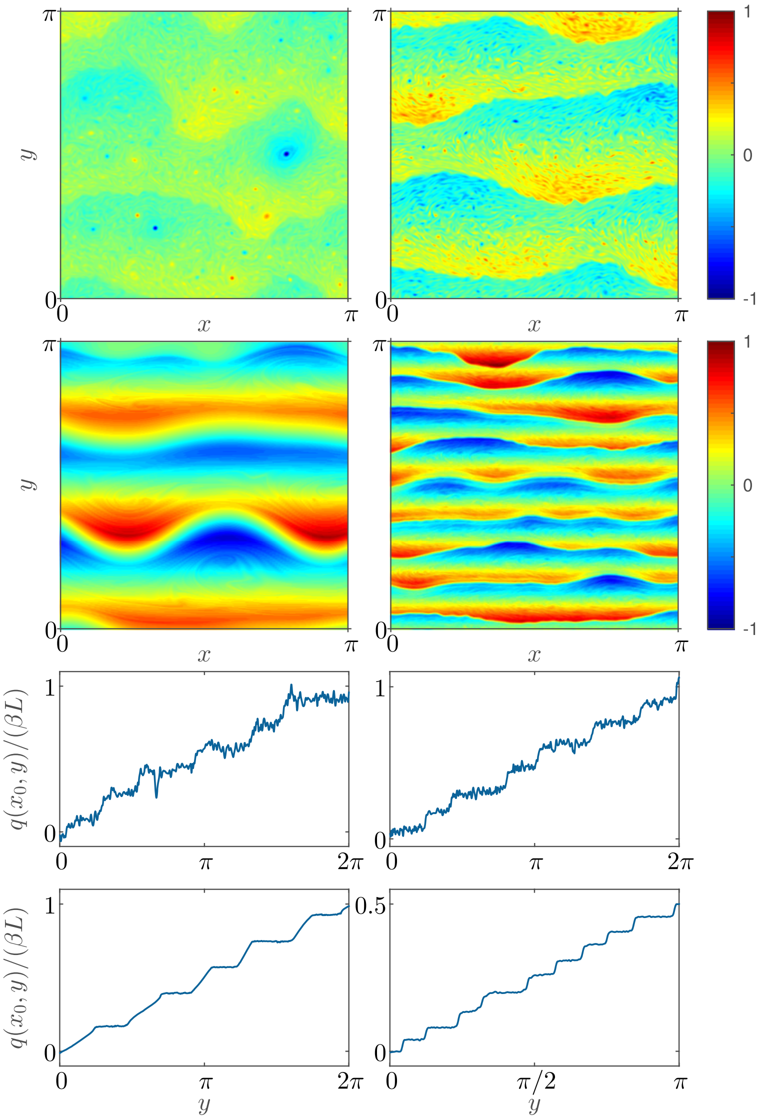

FIG. 3. Snapshots of $q-\beta y$ for simulations 4 and 5 (first row) and simulations 6 and 7 (second row), followed by corresponding meridional profiles of q (final two rows). The snapshots are normalized as in Fig. 1. Each snapshot shows just one quadrant so that small scale features are visible.

First, we again see a NDL which in Sec. III could be fully accounted for by westward propagating vortices. Here, however, only simulations 4 and 5 have vortices. Because there are no other coherent structures, we may deduce for simulations 6 and 7 that the jet meanders propagate westward at an approximately uniform speed.

For the two simulations with both jets and coherent vortices (simulations 4 and 5), the uniform westward propagation of the jet meanders is proven via the Hovmöller diagrams in Fig. 6. Each Hovmöller diagram corresponds to a slice along constant $y = y_0$, with y_0 chosen such that a jet meander is intersected. The boundaries between the bands seen in the Hovmöller diagrams coincide with the locations of jets and have roughly constant slope. Moreover, in each simulation, the slope appears to be independent of y_0, proving that every point along each meander propagates westward at roughly the same speed.

The second interesting spectral feature is the slope of the NDL, which is lower (in magnitude) than the long-wave Rossby speed. That is, jet meanders propagate westward at some speed $|c| < |c_R|$. We calculate the slope of each NDL from the $k\omega$-spectra by finding for each k the value of ω that maximizes $\mathcal{K}(k, \omega)$, resulting in a collection of pairs (k, ω) upon which a linear regression is performed. To check the robustness of the calculation, we follow the same procedure with the roles of k and ω reversed. The two methods give slopes that agree (within error bars) as long as the NDL is sufficiently narrow, a condition satisfied by simulations 4–7 but not by simulations 1–3 in Sec. III. The normalized propagation speeds for simulations 4–7 are $c/c_R = 0.761 \pm 0.011$, 0.958 ± 0.017, 0.706 ± 0.003, and 0.874 ± 0.005. Error estimates are for the 95% confidence interval, so $|c/c_R| < 1$ with high confidence in each case.

In the absence of forcing and dissipation, any solution that propagates with constant zonal speed c (by convention, $c < 0$ implies westward propagation) must satisfy

$$J(\psi + cy, q) = 0, \tag{21}$$

which can be derived from Eq. (1) by making the substitution $\partial_t q = -c\partial_x q$. Equation (21) is satisfied whenever $q = F(\psi + cy)$ for some function F, with the caveat that there may be different functions F in different regions of the flow, with appropriate matching between regions. Spatially localized solutions (sometimes called modons) of Eq. (21) and its analogs have

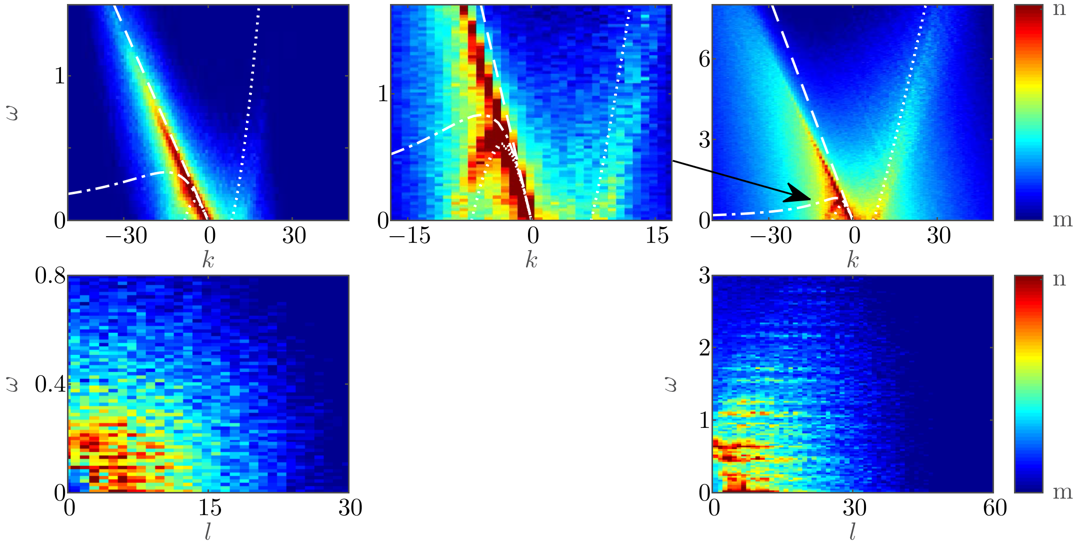

FIG. 4. For simulations 4 (left) and 5 (right), the zonal wavenumber-frequency spectra $\log_{10}[\mathcal{K}(k,\omega)/\mathcal{K}_0]$ (top row) and meridional wavenumber-frequency spectra $\log_{10}[\mathcal{K}(l,\omega)/\mathcal{K}_0]$ (bottom row). As indicated by the arrow, the middle plot shows the $k\omega$-spectra for simulation 5 magnified to better show the additional dispersion relation. The dashed line has a slope equal to the long-wave Rossby speed c_R. The dashed-dotted curve is the ($l = 0$) Rossby dispersion relation, and the dotted curve is the predicted linear dispersion relation given later in Eq. (29). Normalization constants $\mathcal{K}_0$ are as in Fig. 2. The color bar scales are (m, n) = (−4.5, −2), (−6, −3.5), and (−7.5, −3.5) for the top row and (−3.5, −1) and (−6, −2) for the bottom row (left-to-right).

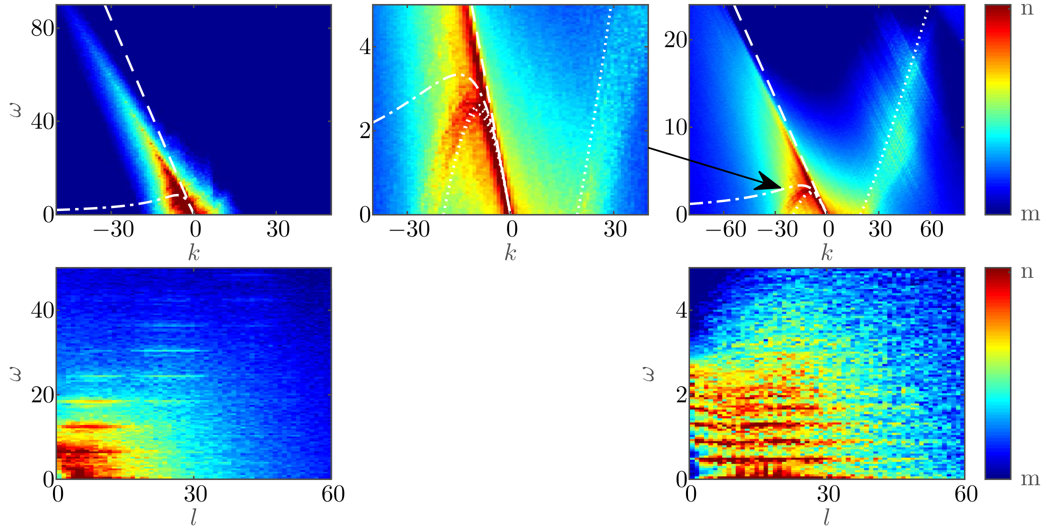

FIG. 5. For simulations 6 (left) and 7 (right), the zonal wavenumber-frequency spectra $\log_{10}[\mathcal{K}(k,\omega)/\mathcal{K}_0]$ (top row) and meridional wavenumber-frequency spectra $\log_{10}[\mathcal{K}(l,\omega)/\mathcal{K}_0]$ (bottom row). As indicated by the arrow, the middle plot shows the $k\omega$-spectra for simulation 7 magnified to better show the additional dispersion relation. The various dashed and dotted curves are as in Fig. 4. Normalization constants $\mathcal{K}_0$ are as in Fig. 2. The color bar scales are (m, n) = (−9, −5), (−8.5, −3.5), and (−9, −4) for the top row and (−9, −2.5) and (−6, −2.5) for the bottom row (left-to-right).

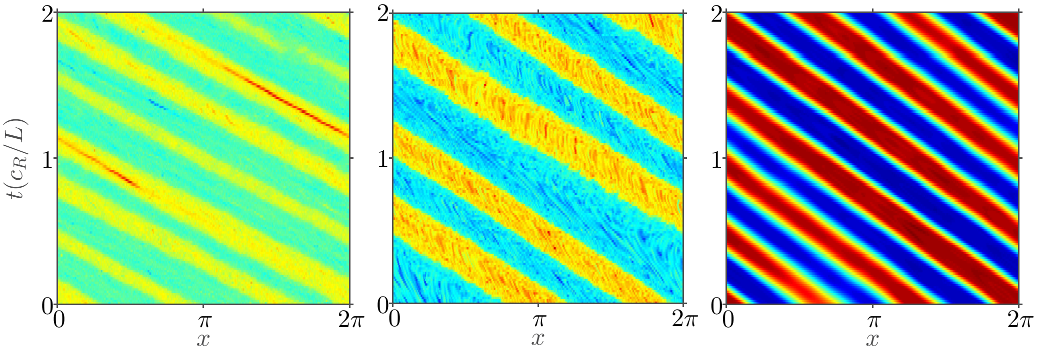

FIG. 6. Hovmöller diagrams of $q - \beta y$ for simulations 4–6 (left to right). Normalization and color scale are the same as for the snapshots in Fig. 3.

been studied for a variety of systems.[37–49] A solution to Eq. (21) that includes jets would not be spatially localized, however.

Figure 7 shows scatter plots of q versus $\psi + cy$ for simulations 6 and 7. The functional form of F for simulation 6 (and maybe simulation 7) appears to be well approximated by a piecewise linear function with two segments per jet: a decreasing linear part $F(\eta) \approx -A\eta + B$ with $A > 0$ and a constant part $F(\eta) \approx Q$. The simplicity of F suggests that an analytical treatment may be possible, but we leave it for future work. Related studies have found finite amplitude wave solutions given other choices for the form of F.[50,51]

Dynamical equations have been derived for the propagation of thin jets assuming various forms of the shallow water equations.[52–56] Because the full shallow water equations admit additional motions not allowed in the quasi-geostrophic model,[57] we cannot apply their results directly here. However, steady westward propagating solutions were derived by Cushman-Roisin, Pratt, and Ralph[55] for a semigeostrophic model (which allows for a finite Rossby number). They found that periodic meanders propagate steadily eastward at speed c if they satisfy

$$\frac{\partial^2\theta}{\partial s^2} + \frac{c+b}{a}\sin\theta = 0, \tag{22}$$

where $\theta(s)$ is the angle of the jet contour (counterclockwise from the x-axis) at coordinate s along the jet, $a > 0$ is a constant, and

$$b := \frac{g'(h_1+h_2)}{2f_0^2}\frac{\partial f}{\partial y}. \tag{23}$$

In Eq. (23), g' is reduced gravity, h_1 and h_2 are layer heights far from the jet on either side, and f is the Coriolis parameter. Making the substitutions $\beta = \partial f/\partial y$, $L_d^2 = g'H/f_0^2$, and $H = (h_1 + h_2)/2$, where H is the average height of the fluid, we get

$$b = \beta L_d^2 = -c_R. \tag{24}$$

Equation (22) has zonally periodic eastward jet solutions only when $(c + b) > 0$, so

$$c > c_R. \tag{25}$$

Because c_R is negative, this means that the jet meanders must propagate westward more slowly than the long-wave Rossby speed (or at any eastward speed) in the semigeostrophic model.

In addition to the NDL, a dispersion relation with both eastward and westward phases and group velocities appears in simulations 4, 5, and 7. In general, this additional dispersion relation appears whenever $k_f > k_d$ (unlike simulation 6 which has $k_f = k_d = 6$) and is limited to the region $k < k_f$. Magnified plots in the middle column of Figs. 4 and 5 show the additional dispersion relation most clearly.

The form of the dispersion relation roughly follows that of linear waves on an idealized zonal PV staircase. It is not obvious that this should be the case, since the actual background flow is not purely zonal (the jets have large meanders). There may be a more general result allowing for non-zonal background flows, and it would be interesting if such a theory could be developed.

We briefly sketch the theory for the zonal case. Let

$$q(x, y, t) = Q(y) + q'(x, y, t), \tag{26}$$

where $Q(y)$ is the zonal background flow and q' is a small perturbation. Motivated by the form of the meridional profiles for simulations 4–7 shown in Fig. 3, we define the background flow to be a zonal PV staircase,

$$Q(y) = \sum_{n=1}^{N} \frac{\beta L}{N} H(y - nW), \tag{27}$$

where $H(y)$ is the unit step function and N is the number of jets. Because the domain height is $L = 2\pi$, the jet spacing is $W = 2\pi/N$. It is a standard exercise to show that the linearized equation of motion admits zonally propagating wave solutions of the form

$$q'(x, y, t) = q'_m(y)e^{-i(kx-\omega t)}, \tag{28}$$

with the dispersion relation

$$\omega = k\Bigg(-\frac{\beta}{k_d^2} + \frac{\beta W}{2k_d\tanh\left(\frac{1}{2}k_d W\right)} - \frac{\beta W}{2K}\left[\tanh\left(\tfrac{1}{2}KW\right) + \frac{2\sin^2\left(\frac{1}{2}mW\right)}{\sinh(KW)}\right]^{-1}\Bigg), \tag{29}$$

where m is any integer and

$$K := \sqrt{k^2 + k_d^2}. \tag{30}$$

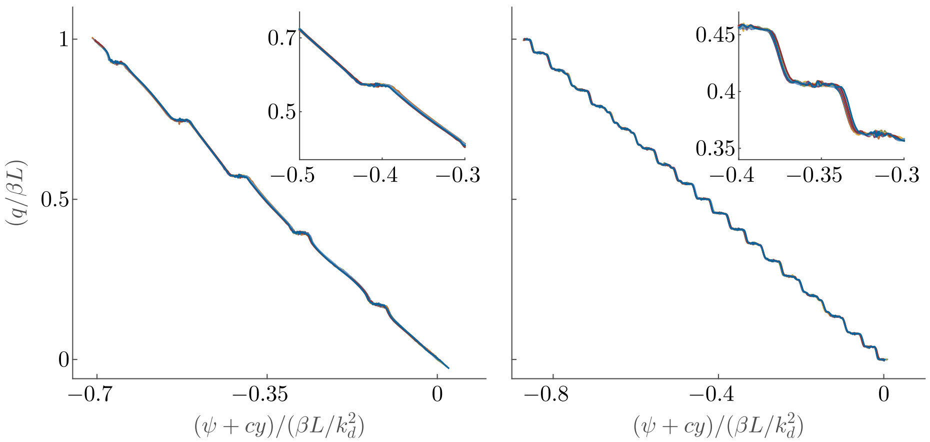

FIG. 7. Potential vorticity q versus $\psi + cy$ for simulations 6 and 7 (left and right). For each plot, a single snapshot is used, and instead of showing all 1024^2 grid points we show eight evenly spaced meridional slices (each a different color). A section of each plot is magnified and shown in an inset. There is much overlap among the eight meridional slices, showing that the functional relationship between q and $\psi + cy$ is relatively unchanged across the domain.

The meridional profile $q'_m(y)$ for each wave solution depends on the integer m, and its explicit form is unimportant here. We use the acronym LWDR to refer to the "linear wave dispersion relation," Eq. (29).

According to Eq. (29), there are multiple modes, each with a different value of m. However, because $0 \leq \sin^2(\frac{1}{2}mW) \leq 1$, we can bound the dispersion relation above and below, and it turns out that the allowed range is narrow. We plot the upper and lower bounds of the dispersion relation for simulations 4–7, noting that they are so close together that they seem to be a single curve. Since the background flow is not purely zonal, there is an expected discrepancy between theory and the simulated spectra. What is interesting is that the theoretical prediction still works reasonably well even though the jets have large meanders.

The $l\omega$-spectra for simulations 4–7 are also shown in Figs. 4 and 5. The noteworthy feature is the presence of horizontal (constant ω) stripes, which arise from the NDL dispersion relation $\omega = ck$ as described in Sec. III. In contrast with simulations 1–3, the NDLs for simulations 4–7 are sufficiently narrow such that the stripes appear in the $l\omega$-spectra. The uniform propagation of the jet meanders explain the NDL and therefore also explain the horizontal stripes. This provides an alternative explanation for the evenly spaced peaks in frequency spectra previously noted by Suhas and Sukhatme.[23]

V. VERY HIGH $\gamma_\beta \gg \gamma_{\beta,crit}$ (NONEQUILIBRATED JETS)

Finally, we consider simulations with γ_β much greater than the threshold for jet formation. These flows have jets and take a very long time to equilibrate. We investigate not only equilibrated but also nonequilibrated simulations because interesting spectral features appear during the slow evolution. In Sec. IV (where $\gamma_\beta \gtrsim \gamma_{\beta,crit}$), the flows develop a NDL and LWDR very early during spin-up and those features persist as the flow equilibrates. In this section (where $\gamma_\beta \gg \gamma_{\beta,crit}$), the flows also eventually develop a PV staircase with NDL and LWDR, but a different dispersion relation appears during spin-up. Because we have already investigated the PV staircase in Sec. IV, in this section we focus on the additional dispersion relation. Due to the excessively long spin-up times, only a selected few simulations with very high γ_β were run long enough to produce a PV staircase.

We present three nonequilibrated cases (simulations 8–10), selected to highlight the additional dispersion. The respective values for γ_β are (15, 20, 30) and for γ_{Rh} are (1.6, 2.3, 3.2). All three simulations have the largest value of $\beta = 1000$ and are forced at relatively small scales with $k_f \in \{30, 90\}$. The other defining parameters are given in Table I.

Figure 8 shows snapshots of $q - \beta y$ and meridional profiles of q. We also show the corresponding meridional profiles of $q - \beta y$, which are relevant to the theory. The jet spacing is narrower than in previous cases, but relative to the jet spacing there is still significant meandering (particularly in simulation 8). The meridional profiles of q take the form $q \approx \beta y$, and while the jets can be seen in the PV profile, they do not take the form of a clear PV staircase. The meridional profiles of $q - \beta y$ are roughly sinusoidal for simulations 8 and 9 but not for simulation 10.

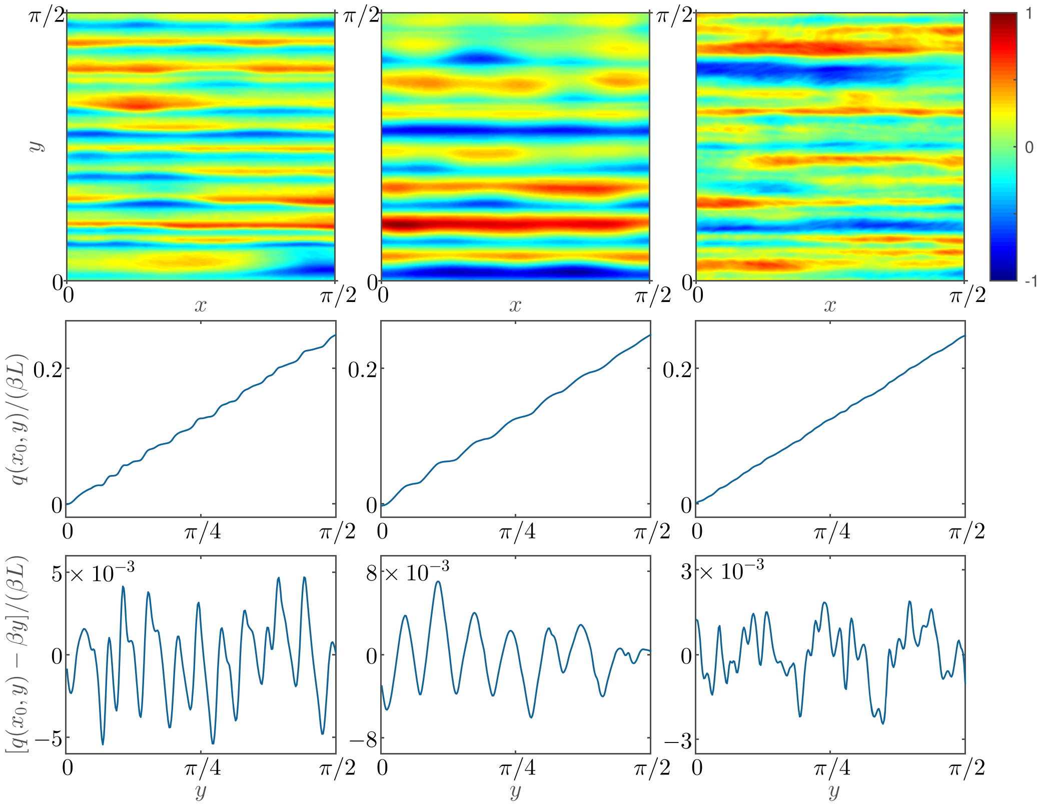

FIG. 8. For simulations 8–10 (left-to-right), snapshots of $q - \beta y$ (top row), corresponding meridional profiles of q (middle row), and meridional profiles of $q - \beta y$ (bottom row). The snapshots are normalized as in Fig. 1. In order to show small-scale features, only a part of each snapshot and profile is shown.

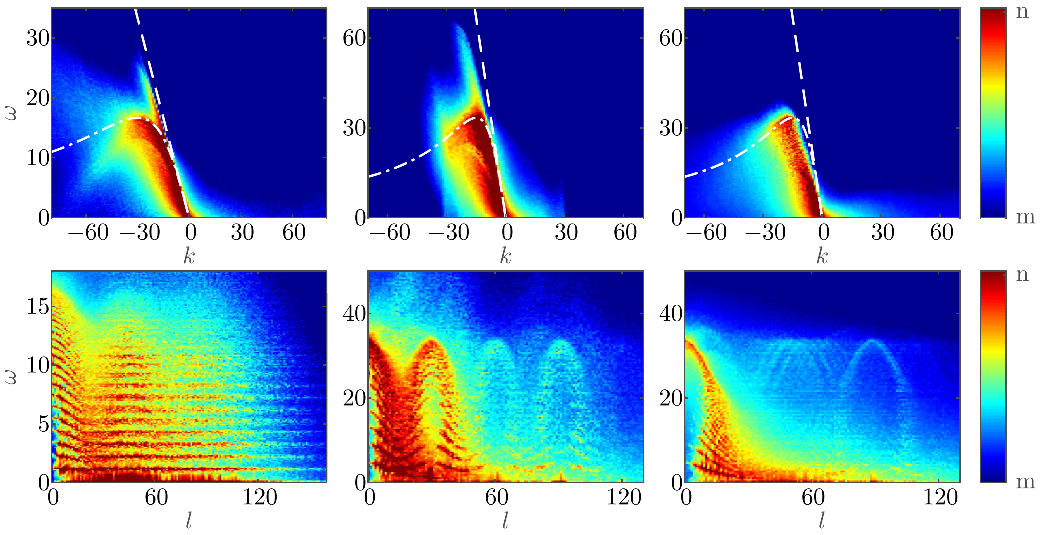

FIG. 9. For simulations 8–10 (left-to-right), the zonal wavenumber-frequency spectra $\log_{10}[\mathcal{K}(k,\omega)/\mathcal{K}_0]$ (top row) and meridional wavenumber-frequency spectra $\log_{10}[\mathcal{K}(l,\omega)/\mathcal{K}_0]$ (bottom row). The dashed and dash-dotted curves are as described in Fig. 2. Normalization constants $\mathcal{K}_0$ are as in Fig. 2. The color bar scales are (m, n) = (−8.5, −5.5), (−9, −5), and (−7, −3) for the top row and (−8, −3.5), (−9.5, −4), and (−8, −1.5) for the bottom row (left-to-right).

The $k\omega$-spectra for simulations 8–10 shown in Fig. 9 still have some energy along a NDL with westward propagation at a speed slower than the long-wave Rossby speed. In contrast with spectra in Sec. IV, the NDL does not extend much beyond the ($l = 0$) Rossby dispersion relation. Significant energy also lies along the ($l = 0$) Rossby dispersion relation and perhaps elsewhere, but little more can be learned from inspection of the $k\omega$-spectra.

The $l\omega$-spectra (also in Fig. 9) provide additional information. In simulation 8, the $l\omega$-spectrum follows the Rossby dispersion relation at low l (one curve for each k) and follows the NDL dispersion relation at high l (one horizontal stripe for each k with $w = ck$). In simulation 9, the $l\omega$-spectra also follows the Rossby dispersion relation at low l but at higher l a different dispersion relation appears. The new dispersion relation is periodic in the l-direction and looks like a periodic extension of the Rossby dispersion relation with period $l_0 \approx 30$. Simulation 10 also shows hints of this new dispersion relation.

Further insight may be gained by considering various slices of $\mathcal{K}(k,l,\omega)$ at fixed k. Figure 10 shows $\mathcal{K}(k_0,l,\omega)$ with $k_0 = -10$ fixed for simulations 8–10. In simulation 8, there is a periodic extension of the Rossby dispersion relation at high l that was not apparent in the $l\omega$-spectra. In that case, the additional dispersion relation coexists with the more dominant NDL. In simulation 9, for which the meridional profile

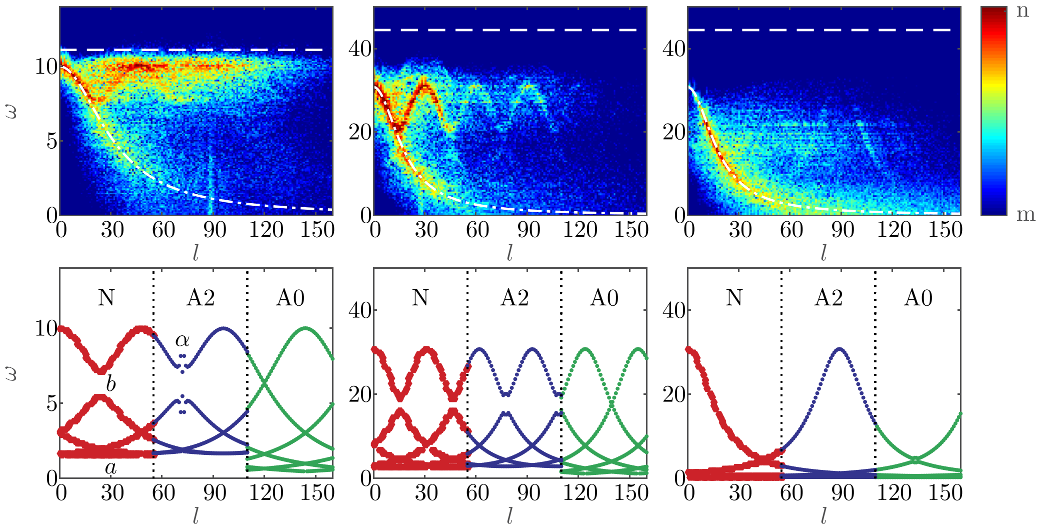

FIG. 10. For simulations 8–10 (left-to-right), slices of the full wavenumber-frequency spectra $\log_{10}[\mathcal{K}(k_0,l,\omega)/\mathcal{K}_0]$ at fixed zonal wavenumber $k_0 = -10$ (top row). The dashed line corresponds to westward propagation at the long-wave Rossby speed c_R, while the dashed-dotted curve is the ($k = k_0$) Rossby dispersion relation. The color bar scales are (m, n) = (−6.5, −1.5), (−7.5, −2.5), and (−7, −1) (left-to-right). The bottom row shows the corresponding theoretical dispersion relations calculated in three ways: numerically (labeled as N), analytically out to second order (A2), and analytically out to zeroth order (A0). All three dispersion relations are periodic over all l but are plotted in non-overlapping regions for clarity: N (red) for $0 \le l < 55$, A2 (blue) for $55 \le l < 110$, and A0 (green) for $l \ge 110$. The labels a and b indicate regions where A2 significantly improves upon A0 as an approximation for N. The label α indicates the region $\ell \approx l_0/2$, where the perturbation expansion can fail when ϵ is finite.

of $q - \beta y$ is the most sinusoidal, the periodically extended Rossby dispersion relation is very clear. In simulation 10, which has multiple periodicities in the meridional profile of $q - \beta y$, the periodically extended Rossby dispersion relation is less well-defined and appears to involve multiple periods.

We show simulations 8 and 9 primarily because they show the periodic dispersion relation most clearly, but they are not representative of most nonequilibrated simulations with high γ_β. More common are $l\omega$-spectra represented by simulation 10, which shows hints of the Rossby dispersion relation extended periodically but with multiple periods. Below we derive the dispersion relation for the case of a single period. The multiple period case is much more complicated mathematically, so we do not consider it here.

The periodic dispersion relation seen in simulations 8 and 9 may be derived by considering a small perturbation to a zonal background flow as in Sec. IV. Whereas before the background flow was a PV staircase, here the background flow is given by

$$Q(y) = Q_0 \sin(l_0 y + \phi_0) + \beta y \tag{31}$$

or, equivalently,

$$U(y) = U_0 \cos(l_0 y + \phi_0), \tag{32}$$

where $U(y)$ is the background zonal velocity; $Q_0 > 0$, $l_0 > 0$ and ϕ_0 are arbitrary constants, and $U_0 := Q_0 l_0/(l_0^2 + k_d^2) > 0$. The phase ϕ_0 is unimportant and is set to zero. Equation (32) can be thought of as a simple model for a background flow where the meridional profile of the zonal velocity is dominated by a single Fourier mode with meridional wavenumber l_0. The linearized equation of motion is

$$q'_t + [Q_0 l_0 \cos(l_0 y) + \beta]\psi'_x + U_0 \cos(l_0 y) q'_x = 0, \tag{33}$$

where ψ' is the perturbation stream function and subscripts t and x indicate partial differentiation.

If in addition the background flow $Q(y)$ is dominated by the β term, meaning that the derivative

$$Q_y(y) = Q_0 l_0 \cos(l_0 y) + \beta \tag{34}$$

is dominated by β, then the nondimensional parameter

$$\epsilon := Q_0 l_0/\beta \tag{35}$$

will be small. Below we consider both finite and infinitesimal ϵ.

For finite ϵ, westward propagating solutions of Eq. (33) can be found numerically using Floquet theory, as has been done in related two-layer and continuously stratified models.[58–61] Alternatively, Eq. (33) can be transformed into Hill's differential equation and then solved numerically by finding the zeros of an infinite determinant.[62–64] Instead, we transform Eq. (33) into a second order recurrence relation, which allows us to derive two key insights for the finite ϵ case and leads to a straightforward numerical method for calculating the dispersion relation. We then derive the dispersion relation perturbatively out to second order for infinitesimal ϵ using the known eigenvalues of the Whittaker-Hill equation.

A zonally propagating solution to Eq. (33) must take the form

$$\psi'(x,y,t) = \sum_{k,l} \widetilde{\psi}'_{k,l} e^{-i(kx+ly-kct)}, \tag{36}$$

where c is the zonal propagation speed. Substitution of Eq. (36) into Eq. (33) gives a second order recurrence relation for the various Fourier modes of the perturbation stream function,

$$\left[c\left(k^2 + l^2 + k_d^2\right) + \beta\right] \widetilde{\psi}'_{k,l} = \frac{1}{2} l_0 Q_0 \left(\frac{k^2 + l^2 - l_0^2}{l_0^2 + k_d^2}\right) \times \left(\widetilde{\psi}'_{k,l+l_0} + \widetilde{\psi}'_{k,l-l_0}\right). \tag{37}$$

For each fixed zonal wavenumber k, Eq. (37) is a recurrence relation indexed by l with step size l_0.

The first useful implication of Eq. (37) is that the dispersion relation will be periodic in l with period l_0 because $\widetilde{\psi}'_{k,l+l_0}$ will typically be nonzero whenever $\widetilde{\psi}'_{k,l}$ and $\widetilde{\psi}'_{k,l-l_0}$ are nonzero. The second useful implication comes from imposing the boundary condition that $\widetilde{\psi}'_{k,l} \to 0$ as $l \to \pm\infty$, a necessary condition for $\psi'(x,y,t)$ to be a well-behaved function. As shown in Appendix A, this boundary condition implies that

$$|c| > U_0. \tag{38}$$

In other words, the linear waves must propagate faster than the maximal zonal velocity within the jet. A numerical method for calculating c using the recurrence relation is also provided in Appendix A and is used in Fig. 10. The numerical method and Eq. (38) are valid regardless of the size of ϵ.

To obtain the dispersion relation perturbatively for small ϵ, we first assume a westward propagating wave of the form

$$\psi'(x,y,t) = P(y) e^{-ik(x-ct)}. \tag{39}$$

Substituting Eq. (39) into the linear wave equation (33) and expanding out to second order in ϵ results in a differential equation for $P(y)$ of the form

$$P_{yy}(y) + \left[\lambda + A\epsilon \cos(l_0 y) + B\epsilon^2 \cos(2 l_0 y)\right] P(y) = 0. \tag{40}$$

The parameters λ, A, and B depend on the propagation speed c and are given explicitly in Appendix B.

Equation (40) is the Whittaker-Hill equation,[65,66] which generalizes the more familiar Mathieu's equation[67] (which has $B = 0$). Similar to Mathieu's equation, the Whittaker-Hill equation has y-periodic solutions (with period 2π) only for certain discrete eigenvalues λ. Perturbation expansions for the eigenvalues and eigenvectors are known.[68] From the perturbation expansions for λ, we obtain perturbation expansions for the westward propagation speed,

$$c = c_0 + c_1\epsilon + c_2\epsilon^2 + O\left(\epsilon^3\right), \tag{41}$$

accurate out to second order. We provide the calculation details in Appendix B and summarize the results below.

For integer ℓ with $|\ell| \neq l_0/2$ and $|\ell| \neq l_0$ (i.e., for most ℓ), the propagation speed is

$$c = \frac{-\beta}{k^2 + \ell^2 + k_d^2} + \frac{\epsilon^2}{2}\beta \frac{\left(k^2 + \ell^2 - l_0^2\right)\left(k^2 - 3\ell^2\right)}{\left(l_0^2 + k_d^2\right)^2\left(4\ell^2 - l_0^2\right)} + O\left(\epsilon^3\right). \tag{42}$$

The integer ℓ is the meridional wavenumber of the zeroth-order solution, which is a Rossby wave. Because the full dispersion relation is periodic in l with period l_0 [as explained below Eq. (37)], the full dispersion relation is obtained by letting

$$\ell := l + ml_0 \tag{43}$$

in Eq. (42), for every integer m.

According to Eqs. (42) and (43), the leading order propagation speed c_0 periodically extends the Rossby dispersion relation in the l-direction with period l_0. As $\epsilon \to 0$, the stream function perturbation ψ' approaches a Rossby wave, but the dispersion relation does not approach the Rossby dispersion relation, due to the periodic extension. The next order coefficient c_1 is zero, so the periodically extended Rossby dispersion relation is a good approximation when ϵ is small and c_2 is not too large.

While Eq. (42) is correct for infinitesimal ϵ, when ϵ is finite the perturbation expansion for c cannot be trusted wherever c_2 approaches infinity, which happens as $\ell \to \pm l_0/2$ and as $\ell \to \pm\infty$. To avoid the latter, we plot the dispersion relation only for $|\ell| \leq 5l_0/2$ in Fig. 10. We also indicate in Fig. 10 the region $\ell \approx l_0/2$, where indeed the second order correction appears to fail when ϵ is not sufficiently small.

Finally, note that while Eq. (42) gives the propagation speed c for most integers ℓ, there are two special cases: $|\ell| = l_0/2$ and $|\ell| = l_0$. For completeness, the perturbation expansions for c for these additional cases are given in Appendix A. However, their effects on the full dispersion relation are small and isolated. The only noticeable effect in Fig. 10 occurs at $\ell = l_0/2$ (indicated by the label α) in simulation 8, which has relatively large ϵ.

The bottom row of Fig. 10 shows the numerically calculated and analytically derived dispersion relations for simulations 8–10 with $k_0 = -10$ and with (l_0, ϵ) = (48, 0.5), (31, 0.3), and (89, 0.18), respectively. For the analytically derived dispersion relation, going out to second order improves the agreement with the numerically calculated dispersion relation, particularly in the regions marked a and b. The predicted lower bound on c given by Eq. (38) combined with $\omega = ck$ gives the bound

$$|\omega| > U_0|k_0|. \tag{44}$$

The gap above $\omega = 0$ (region a) is consistent with this bound and can also be seen in the simulation spectra: as the predicted gap size increases (right-to-left in Fig. 10), less energy is found near $\omega = 0$ in the simulation spectra. The separation between upper and lower dispersion relations (region b) is also somewhat noticeable in the simulation spectra.

To obtain the model values l_0 and ϵ from the simulation output, we first define $q_- := q - \beta y$, which has spatial Fourier transform $\widetilde{q_-}(k, l)$. We then select l_0 that maximizes $\epsilon(l) := l|\widetilde{q_-}(0, l)|/\beta$. For simulation 8, the three largest values of $\epsilon(l)$ are $\epsilon(48) = 0.17$, $\epsilon(45) = 0.13$, and $\epsilon(47) = 0.11$; for simulation 9, the three largest values of $\epsilon(l)$ are $\epsilon(31) = 0.3$, $\epsilon(30) = 0.16$, and $\epsilon(29) = 0.09$. In both cases, the function $\epsilon(l)$ has a single narrow peak. However, for simulation 10, the two largest values are $\epsilon(89) = 0.06$ and $\epsilon(58) = 0.05$, so there is no single narrow range of l that dominates. In every case instead of a single dominate mode l_0, there are one or more narrow ranges of l that dominate. To obtain a single value for ϵ, we set $\epsilon = \sqrt{\sum_l |\epsilon(l)|^2}$. This choice gives a more accurate dispersion relation than if we simply set $\epsilon = \epsilon(l_0)$. Although the sum is over all l, only a few terms within a narrow range contribute substantially to the sum when there is a single dominant peak (as in simulations 8 and 9). For simulation 10, which has multiple peaks, ϵ is so small that the choice to sum over all l has practically no effect on the dispersion relation.

VI. DISCUSSION

In summary, a numerical investigation of Eq. (1) with emphasis on wavenumber-frequency spectra reveals interesting and previously unexamined phenomena. Perhaps the most interesting result is the persistence of the NDL—indicating uniform westward propagation—as γ_β is increased beyond the threshold for jet formation.

We have shown that not only coherent vortices but also jet contours propagate roughly uniformly westward for a wide range of simulation parameters. Uniform westward propagation of the jets happens whenever the flow may be approximated by a PV staircase, which appears to be the case for all equilibrated simulations with jets. The PV staircases are nonzonal in the sense that meridional excursions of the jets are usually much greater than the jet widths. The meridional excursions are also typically of the same order as the jet spacing. While coherent vortices propagate roughly at the long-wave Rossby speed, the jet meanders propagate westward more slowly. Scatter plots of q versus $\psi + cy$ appear to be approximately piecewise linear, providing a simple model for future work on the dynamics of uniformly propagating jets.

When γ_β (or γ_{Rh}) is above the threshold for jet formation, wavenumber-frequency spectra show not only a NDL but other spectral features as well. When the background flow is a PV staircase with large meanders, the additional dispersion relation, denoted as LWDR, roughly follows that of linear waves on a zonal PV staircase. The dispersion relation is close to the Rossby dispersion relation at small l, but it curves more sharply, leading to eastward phase and group velocities at large l.

For very large γ_β, when the flow has not equilibrated and the background PV gradient is dominated by the β term, yet another dispersion relation appears. The dispersion relation is either periodic in the l-direction or has multiple periodicities, depending on the relative magnitudes of the various modes in the Fourier decomposition of the background flow. We have shown that a simple model that treats the perturbation as a sinusoid accurately predicts the additional dispersion relation seen in the very large γ_β simulations.

Figure 11 provides a summary of all simulations with $\beta \neq 0$ and elucidates the relationship between γ_β and γ_{Rh}. The parameter ranges for the various flow features (vortices, jets, NDL, and LWDR) are also indicated in the figure. The threshold for jet formation appears to be $\gamma_{\beta,crit} = 1.3 \pm 0.15$, remarkably consistent with the predicted value of $\gamma_{\beta,crit} = 1.3$. However, γ_{Rh} for simulation 3 exceeds γ_{Rh} for simulation 4, even though the latter has jets while the former does not, so there is no well-defined threshold $\gamma_{Rh,crit}$ above which jets form. All simulations with $\gamma_{Rh} > 0.75$ have jets, while all simulations with $\gamma_{Rh} < 0.54$ do not. A value of $\gamma_{Rh,crit} = 0.65$ can be used to indicate roughly where the transition to jets occurs.

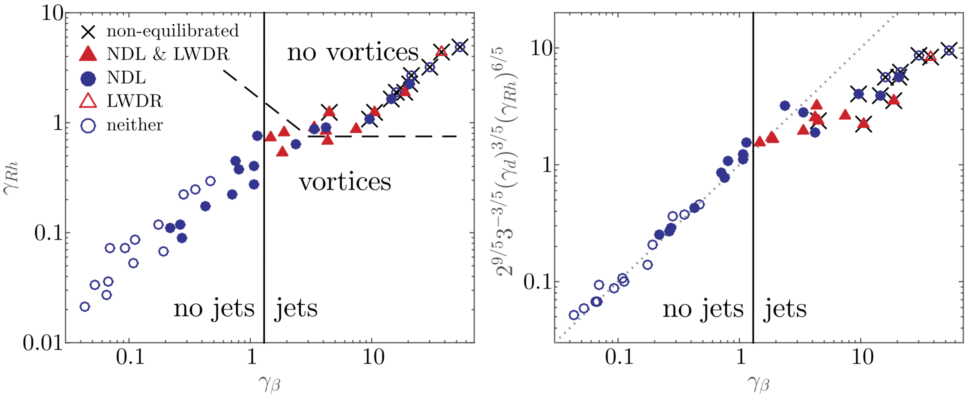

FIG. 11. Scatter plots show the relationship between γ_{Rh} and γ_β, as well as the various flow regimes for all 54 simulations (except for the 6 simulations with $\beta = 0$). The physical and spectral features for each simulation were determined subjectively by visually inspecting snapshots and spectra. The vertical solid line at $\gamma_\beta = 1.3$ corresponds to the threshold for jet formation. The dashed line separates runs with and without vortices. The dotted line in the right panel corresponds to the prediction $\gamma_\beta = 2^{9/5}3^{-3/5}\gamma_d^{3/5}\gamma_{Rh}^{6/5}$ derived in Appendix C.

The left panel in Fig. 11 shows γ_{Rh} versus γ_β and has significant scatter because there is no one-to-one relationship between γ_β and γ_{Rh}. A relationship between γ_β and γ_{Rh} can be derived by assuming a form for the isotropic wavenumber spectra $\mathcal{K}(\kappa)$. One can show that

$$\gamma_\beta = g(\gamma_d, \gamma_f)(\gamma_{Rh})^{6/5}, \tag{45}$$

where the function g depends on the model for $\mathcal{K}(\kappa)$ and is derived in Appendix C. Because g varies with either γ_d or γ_f (or both, depending on the spectrum model), we can vary γ_β while holding γ_{Rh} constant (and vice versa). Therefore, if γ_β determines the transition to jets, then γ_{Rh} cannot (and vice versa). In other words, at most one of the two parameters can determine the transition to jets. Given the discussion in the preceding paragraph, it seems likely that γ_{Rh} does not determine the transition to jets while γ_β possibly does.

The right panel in Fig. 11 shows $g(\gamma_d)(\gamma_{Rh})^{6/5}$ versus γ_β, where the factor $g(\gamma_d)$ is derived in Appendix C and is based on a spectral slope of −3 for the kinetic energy. Using the normalized axes, the relationship is nearly one-to-one for simulations without jets. The wavenumber spectra in simulations with jets do not follow a power law because zonal jets lead to evenly spaced peaks in wavenumber spectra.[69] Therefore, the derived relationship between γ_β and γ_{Rh} does not apply to simulations with jets.

The other nondimensional parameters, γ_d and γ_f, determine the widths of the potential and kinetic energy cascades, respectively. While these parameters surely affect some flow characteristics (such as spectral slopes and the ratio of potential to kinetic energy), we do not find much effect on the presence versus absence of jets or the various spectral features seen in wavenumber-frequency spectra. Mainly, the effect of γ_f is to set the size of the coherent vortices. The two linear dispersion relations only appear when $\gamma_f \gtrsim 2$ and only at wavenumbers $\kappa < k_f$, apparently because relatively small-scale forcing is needed to provide the perturbation to the background flow. In contrast, the NDL extends well beyond $\kappa = k_f$ when k_f is small.

Our model and parameter choices may be relevant to Earth's ocean and atmosphere as well as the atmospheres of giant gas planets. At mid-latitudes in Earth's ocean, $\beta \approx 2 \times 10^{-11}$ m^{-1} s^{-1}, $L_d \approx 3$–5×10^4 m,[70] and $U_{rms} \approx 10$ cm s^{-1},[71] so $k_{Rh} \approx 10^{-6}$ m^{-1}. Combining k_{Rh} with L_d gives $\gamma_{Rh} \approx 0.3 - 0.5$, which is slightly below the threshold for jet formation ($\gamma_{Rh,crit} \approx 0.65$). Therefore, we would expect most of the ocean to be dominated by vortices rather than jets, keeping in mind our somewhat narrow definition of "jets" given earlier.

Indeed, Klocker *et al.*[72] recently constructed a regime diagram for geostrophic turbulence in the ocean based on sea surface height measurements over much of the Pacific Ocean. One axis of their regime diagram is the "nonlinearity parameter" defined by Chelton, Schlax, and Samelson,[36]

$$r = \frac{U_{eddy}}{\beta L_d^2}, \tag{46}$$

where U_{eddy} is the root-mean-square eddy velocity. Equating U_{rms} with U_{eddy} (we assume no mean flow) gives the relation

$$\frac{1}{r} = 2\gamma_{Rh}^2. \tag{47}$$

The approximate threshold for jet formation found in our simulations at $\gamma_{Rh} \approx 0.65$ corresponds to $r \approx 1.2$. According to the regime diagram in the work of Klocker *et al.*,[72] regions with $r < 1.2$ can be found near the tropics, while all other regions have $r > 1.2$. Thus, values of γ_{Rh} both above and below the threshold for jet formation are relevant to the ocean.

To obtain γ_β for the ocean, we estimate $\epsilon = 10^{-11}$ m^2 s^{-3}–10^{-9} m^2 s^{-3} for the energy injection rate,[15] where the smaller value comes from the work of Nakano and Hasumi.[73] This gives $\gamma_\beta \approx 0.4$-1.8, which spans the critical value $\gamma_{\beta,crit} = 1.3$, indicating that jets may be possible in some regions, consistent with the work of Nakano and Hasumi.[73] We note that simulations with $\gamma_\beta < \gamma_{\beta,crit}$ produce NDLs most similar (in terms of length and width) to the NDLs seen in oceanic spectra[2] and the eddy-seeded simulations of Early, Samelson, and Chelton.[26]

At mid-latitudes in Earth's atmosphere, again $\beta \approx 2 \times 10^{-11}$ m^{-1} s^{-1}. The deformation radius and Rhines scale k_{Rh}^{-1} in the upper troposphere tend to be roughly equal, with the Rhines scale somewhat smaller than the deformation radius (e.g., Ref. 74), so $k_{Rh} \gtrsim k_d$, which implies that $\gamma_{Rh} \gtrsim 1$.

Bakas and Ioannou[75] estimate that $\epsilon \approx 3 \times 10^{-4}$ m^2 s^{-3} near the tropopause, which gives $\gamma_\beta \approx 1.1$. These estimates for γ_{Rh} and γ_β both lie near the critical values for jet formation, so both vortex-like (weather systems) and jet-like (jet stream) features can be expected.

At mid-latitudes on Jupiter, $\beta \approx 2.5 \times 10^{-12}$ m^{-1} s^{-1} and $L_d \approx 3 \times 10^6$ m, based on a mean layer depth of 20 km.[76] Galperin *et al.*[77] determined that $U_{rms} \approx 50$ ms^{-1} and $\epsilon \approx 10^{-5}$ m^2 s^{-3}. These values give $\gamma_{Rh} \approx 0.4$ and $\gamma_\beta \approx 1.7$, which both lie near the critical values for jet formation. Indeed, Okuno and Masuda[20] found that Jupiter's atmosphere has both regions with $\gamma_{Rh} < 1$ and $\gamma_{Rh} > 1$ and that storm tracks predominately lie within the regions with $\gamma_{Rh} < 1$ (although they define γ_{Rh} somewhat differently, taking into account a nonzero mean zonal flow). Galperin *et al.*[77] also calculate the zonostrophy index $R_\beta := k_\beta/k_{Rh} = \gamma_\beta/\gamma_{Rh}$ on Jupiter to be roughly $R_\beta \approx 5$, which lies within the range of our parameter sweep.

Our investigation has been necessarily limited both by the assumptions of the model and by the breadth of the parameter search. One such limitation is the choice of large-scale dissipation by thermal damping. A linear drag (or a combination of the two) would also have been a reasonable choice. Changing to linear drag would likely affect the steepness of the isotropic wavenumber spectra at large scales and shift the dissipation range to somewhat smaller scales.[21] However, we would still expect the same linear dispersion relations to develop so long as the linear drag is sufficiently weak. Both linear dispersion relations derived in this paper are based on assumed forms of the background flow. In Sec. IV, the background flow is a PV staircase, which is known to also arise in equilibrated simulations with linear drag, even when the deformation radius is infinite.[78,79] In Sec. V, the background flow forms at early times during spin-up, long before the large-scale dissipation is reached.

Lastly, the 1.5-layer system studied here provides only a very rough model for oceanic and atmospheric dynamics. If one is primarily concerned with improving relevance to the ocean, adding a second layer along with a linear drag would be the next logical step. It would be interesting to know whether the NDL also persists when γ_β is increased beyond the threshold for jet formation in a two-layer or more realistic ocean model. Concerning the atmospheres of the gas giants, one might instead consider imposing a nonzero mean zonal velocity to mimic deep zonal jets, as in the work of Thomson and McIntyre.[80]

ACKNOWLEDGMENTS

A.J.M. would like to thank Charles Doering, Robert Deegan, and John Boyd, for providing feedback on this research when it was a chapter in A.J.M.'s dissertation. A.J.M. and B.K.A. gratefully acknowledge Mike Messina for support of the numerical simulations, which were carried out on the supercomputer provided by the University of Michigan Office of Research Cyberinfrastructure (ORCI). We also thank the reviewers for their helpful comments, which greatly improved the manuscript. A.J.M. and B.K.A. acknowledge support from National Science Foundation (NSF) Grant Nos. OCE-0960820 and OCE-1351837 and University of Michigan faculty startup funds. G.R.F. received support from NSF Grant No. OCE-0960826.

APPENDIX A: RECURRENCE RELATION RESULTS AND NUMERICAL METHOD

The recurrence relation equation (37) has the form

$$a_l v_l + b_l (v_{l+l_0} + v_{l-l_0}) = 0, \tag{A1}$$

where $v_l := \widetilde{\psi'}_{k,l}$ and the coefficients a_l and b_l can be read directly from Eq. (37). Equation (A1) has been shown to have solutions only if the coefficients satisfy a particular eigenvalue equation.[81] Below we provide a simple method for obtaining the eigenvalues numerically, and in the process we obtain a theoretical lower bound for the westward propagation speed c.

Because the step size of the recurrence is l_0, there are in fact l_0 independent recurrence relations, one for each $l \in \{0, 1, 2, \ldots, l_0 - 1\}$. Fix some $l' \in \{0, 1, 2, \ldots, l_0 - 1\}$ and define $V_n := v_{l'+nl_0}$, $A_n := a_{l'+nl_0}$, and $B_n := b_{l'+nl_0}$. Then the recurrence relation may be written in the vector form as

$$\begin{pmatrix} V_{n+1} \\ V_n \end{pmatrix} = \begin{bmatrix} 2p_n & -1 \\ 1 & 0 \end{bmatrix} \begin{pmatrix} V_n \\ V_{n-1} \end{pmatrix} \tag{A2}$$

or more compactly as

$$\boldsymbol{V}_{n+1} = M_n \boldsymbol{V}_n, \tag{A3}$$

where $2p_n := -A_n/B_n$.

In order for ψ' to be well-behaved, we impose the boundary condition $\widetilde{\psi}'_{k,l} \to 0$ as $l \to \pm\infty$, which implies that $|\boldsymbol{V}_n| \to 0$ as $n \to \pm\infty$. When $|n|$ is large, p_n approaches

$$p_\infty := \lim_{|n|\to\infty} p_n = \frac{c}{U_0}, \tag{A4}$$

so the eigenvalues of M_n approach

$$\lambda_\pm := p_\infty \pm \sqrt{p_\infty^2 - 1} \tag{A5}$$

as $|n| \to \infty$. Requiring that $|\boldsymbol{V}_n| \to 0$ implies that at least one of the eigenvalues must have magnitude $|\lambda_\pm| < 1$, which happens precisely when $|p_\infty| > 1$ or equivalently when

$$|c| > U_0. \tag{A6}$$

In other words, the linear waves must propagate faster than the maximal zonal velocity within the jet.

For the numerical method, one chooses some very large N (we use $N = 200$) and sets

$$\boldsymbol{V}_N = \boldsymbol{V}_\infty \quad \text{and} \quad \boldsymbol{V}_{-N} = \boldsymbol{V}_{-\infty}, \tag{A7}$$

where $\boldsymbol{V}_{\pm\infty}$ is the eigenvector that decays as $n \to \pm\infty$. A parameter sweep of c is conducted. For each c, one uses the recurrence relation (A3) to calculate $\boldsymbol{V}_0$ from both $\boldsymbol{V}_N$ and $\boldsymbol{V}_{-N}$. If the direction of the two vectors $\boldsymbol{V}_0$ coincides, then c is a special value that admits a solution. To obtain the full spectrum, this procedure is carried out independently for each $l' \in \{0, 1, 2, \ldots, l_0 - 1\}$.

APPENDIX B: PERTURBATION RESULTS FOR THE WHITTAKER-HILL EQUATION

Substituting the westward propagating wave [Eq. (39)] into the linear wave equation (33) gives

$$P_{yy}(y) - \frac{c\left(k^2+k_d^2\right) + \beta + \epsilon\frac{\beta(l_0^2-k^2)}{l_0^2+k_d^2}\cos(l_0 y)}{c - \epsilon\frac{\beta}{l_0^2+k_d^2}\cos(l_0 y)} P(y) = 0, \tag{B1}$$

an exact result for any ϵ. When ϵ is small, Eq. (B1) can be expanded perturbatively out to second order, resulting in the Whittaker-Hill equation [Eq. (40)] with the following coefficients:

$$A := -\frac{\beta}{c}\left[1 + \frac{\beta}{c\left(l_0^2+k_d^2\right)}\right], \tag{B2}$$

$$B := \frac{\beta}{2c\left(l_0^2+k_d^2\right)}A, \tag{B3}$$

$$\lambda := -\frac{\beta}{c} + \left(k^2+k_d^2\right) + B\epsilon^2. \tag{B4}$$

Perturbation expansions for the eigenvalues and eigenvectors are known[68] and are parameterized by integer ℓ. The integer ℓ is the meridional wavenumber of the zeroth order solution,

$$P(y) = C_+ e^{i\ell y} + C_- e^{-i\ell y} + O(\epsilon), \tag{B5}$$

where C_+ and C_- are suitably chosen constants.

When $|\ell| \neq l_0/2$ and $|\ell| \neq l_0$ (i.e., for most ℓ), the eigenvalues are

$$\lambda = \ell^2 + \frac{A^2\epsilon^2}{8\left[\ell^2 - (l_0/2)^2\right]} + O\left(\epsilon^4\right). \tag{B6}$$

Substituting the expressions for A, B, and λ given by Eqs. (B2)–(B4) into Eq. (B6) and solving perturbatively for c gives (after a fair amount of algebra) the main result, Eq. (42).

While the above derivation gives the propagation speed for most ℓ, there are two special cases: $|\ell| = l_0/2$ and $|\ell| = l_0$. For completeness, we provide the perturbation expansions for those two cases here. When $|\ell| = l_0/2$, there are two eigenvalues,

$$\lambda = (l_0/2)^2 \pm \frac{1}{2}A\epsilon - \frac{1}{8l_0^2}A^2\epsilon^2 + O\left(\epsilon^3\right). \tag{B7}$$

In that case, solving perturbatively for c gives

$$c = \frac{-\beta}{k^2+(l_0/2)^2+k_d^2} \pm \frac{\beta\left(4k^2-3l_0^2\right)}{2\left(l_0^2+k_d^2\right)\left(4k^2+l_0^2+4k_d^2\right)}\epsilon - \frac{\beta\left(4k^2-3l_0^2\right)\left(4k^2+5l_0^2\right)}{128\left(l_0^2+k_d^2\right)^2 l_0^2}\epsilon^2 + O\left(\epsilon^3\right). \tag{B8}$$

When $|\ell| = l_0$, there are also two eigenvalues,

$$\lambda = l_0^2 + \frac{(2\pm 3)}{12l_0^2}A^2\epsilon^2 \mp \frac{1}{2}B\epsilon^2 + O\left(\epsilon^4\right). \tag{B9}$$

The corresponding perturbation expansion for c is

$$c = \frac{-\beta}{k^2+l_0^2+k_d^2} + \frac{\beta k^2\left[(2\pm 3)k^2 - (6\pm 3)l_0^2\right]}{12\left(l_0^2+k_d^2\right)^2 l_0^2}\epsilon^2 + O\left(\epsilon^3\right). \tag{B10}$$

These special cases only apply for a few isolated values of ℓ, so their effect on the full dispersion relation is relatively minor. For all other ℓ, the dispersion relation is given by Eq. (42).

Finally, note that in the standard formulation of the Whittaker-Hill equation, the arguments of the cosine terms are typically $2y$ and $4y$, whereas here the arguments are $l_0 y$ and $2l_0 y$. A simple change of variables converts between the two formulations. In the standard formulation, the two special cases occur at wavenumbers 1 and 2, which in our formulation correspond to wavenumbers $l_0/2$ and l_0, respectively. Moreover, every ℓ that is not a multiple of $l_0/2$ in our formulation corresponds to a non-integer wavenumber in the standard formulation. In other words, most of the eigenvalues λ considered above correspond to non-integer order solutions of the Whittaker-Hill equation, which are analogous to non-integer order solutions of Mathieu's equation.[67]

APPENDIX C: RELATIONSHIP BETWEEN γ_β AND γ_{Rh}

We derive the relationship between γ_β and γ_{Rh} based on a model for the isotropic wavenumber spectrum $\mathcal{K}(\kappa)$. Given $\mathcal{K}(\kappa)$, one can calculate the root-mean-square velocity,

$$U_{rms} = \left[2\int d\kappa\, \mathcal{K}(\kappa)\right]^{1/2}, \tag{C1}$$

which gives

$$\gamma_{Rh} = \sqrt{\beta/2U_{rms}}/k_d = 2^{-3/4}\beta^{1/2}k_d^{-1}\left[\int d\kappa\, \mathcal{K}(\kappa)\right]^{-1/4}. \tag{C2}$$

By definition,

$$\gamma_\beta = \mathcal{C}^{-3/10}\beta^{3/5}\epsilon^{-1/5}k_d^{-1}, \tag{C3}$$

so

$$\gamma_\beta = \gamma_{Rh}^{6/5}\left(2^{9/10}\right)\left[\mathcal{C}^{-1}\epsilon^{-2/3}k_d^{2/3}\int d\kappa\, \mathcal{K}(\kappa)\right]^{3/10}. \tag{C4}$$

Standard scaling arguments give a model spectrum of the form

$$\mathcal{K}(\kappa) = \mathcal{C}\epsilon^{2/3}\begin{cases} \kappa^{-5/3}, & k_{DISS} \le \kappa \le k_f, \\ k_f^{4/3}\kappa^{-3}, & k_f \le \kappa \le k_{diss}, \\ 0, & \text{otherwise}, \end{cases} \tag{C5}$$

where k_{DISS} and k_{diss} are sharp cutoffs roughly mimicking large-scale and small-scale dissipation, respectively. However, the actual slope in the inverse cascade range for equilibrated simulations tends to be significantly steeper than −5/3, perhaps because of our choice of hypoviscosity. Because of the steep slope, only the region $k_{DISS} \le k \le k_f$ contributes substantially to the integral. Assuming a slope of $-n$ for the inverse cascade, a reasonable model for $\mathcal{K}(\kappa)$ is therefore

$$\mathcal{K}(\kappa) = \mathcal{C}\epsilon^{2/3}\begin{cases}\kappa^{-5/3}(\kappa/k_d)^{-n+5/3}, & k_{DISS} \leq \kappa,\\ 0, & \text{otherwise.}\end{cases} \tag{C6}$$

The factor (κ/k_d) is used rather than (κ/k_f) or (κ/k_{DISS}) because it gives the best fit in Fig. 11.

With $\mathcal{K}(\kappa)$ given by Eq. (C6), the integral in Eq. (C4) gives

$$\gamma_\beta = 2^{9/10}\left[\frac{1}{n-1}\left(\frac{k_d}{k_{DISS}}\right)^{n-1}\right]^{3/10}\gamma_{Rh}^{6/5}. \tag{C7}$$

We need to express k_d/k_{DISS} in terms of the nondimensional parameter $\gamma_d = k_d/k_{PE}$, which can be accomplished by calculating k_{PE} using Eq. (4). The result is

$$\gamma_d = \left(\frac{n}{n+1}\right)\frac{k_d}{k_{DISS}}, \tag{C8}$$

so

$$\gamma_\beta = g(\gamma_d)\gamma_{Rh}^{6/5}, \tag{C9}$$

where

$$g(\gamma_d) = 2^{9/10}\left[\frac{1}{n-1}\left(\frac{n+1}{n}\right)^{n-1}\gamma_d^{n-1}\right]^{3/10}. \tag{C10}$$

The choice $n = 3$ fits that spectra reasonably well and is used for Fig. 11. Note that if we had used the spectral model given by Eq. (C5), then g would also depend on γ_f.

APPENDIX D: NUMERICAL FORCING

For $\mathcal{F}$, we use a forcing first defined by Lilly,[82] modified to be statistically radially symmetric in wavenumber space as in the work of Maltrud and Vallis.[83] For each wavevector (k, l), the force at discrete time $t = t_n = n\Delta t$ is defined in terms of the force at the previous time-step,

$$\widetilde{\mathcal{F}}(k,l,t_n) = R\widetilde{\mathcal{F}}(k,l,t_{n-1}) + \widetilde{\mathcal{F}}_0(k,l)\sqrt{1-R^2}e^{i\phi_n(k,l)}, \tag{D1}$$

where $\{\phi_n(k,l)\}_{n=0}^{\infty}$ is a set of independent, identically distributed random phases on the interval $[0, 2\pi)$.

This forcing has two adjustable parameters: the real-valued function $\widetilde{\mathcal{F}}_0(k,l)$ controls the expected amplitude of the forcing, while $R \in [0,1]$ controls the integral time scale. To create a narrowband forcing, we define

$$\widetilde{\mathcal{F}}_0(k,l) := A\left((k_f+\Delta k_f)^2-\kappa^2\right)\left(\kappa^2-(k_f-\Delta k_f)^2\right) \tag{D2}$$

for $|\kappa - k_f| < \Delta k_f$, and $\widetilde{\mathcal{F}}_0(k,l) := 0$ for all other κ. The amplitude A is chosen such that

$$\frac{1}{N^4}\sum_{k,l}\left|\widetilde{\mathcal{F}}_0(k,l)\right|^2 = 1, \tag{D3}$$

where $N^2 = 1024^2$ is the simulation resolution. Parseval's theorem then implies that the spatial average of $|\mathcal{F}_0(x,y)|^2$ is unity, which in turn implies that the expectation value of $|\mathcal{F}(x,y,t_n)|^2$ is also unity. The width of the narrowband forcing is set to $\Delta k_f = 2$ in all simulations.

The parameter R determines the integral time scale. The case $R = 0$ corresponds to white noise forcing, while the case $R = 1$ corresponds to constant forcing. The integral time scale is $\tau = 0.5\Delta t(1+R)/(1-R)$, where Δt is length of a single time step. We set $\tau = 0.1$ in all simulations.

[1] D. B. Chelton and M. G. Schlax, "Global observations of oceanic Rossby waves," Science **272**, 234–238 (1996).
[2] C. Wunsch, "The oceanic variability spectrum and transport trends," Atmos.-Ocean **47**, 281–291 (2009).
[3] B. K. Arbic, R. B. Scott, G. R. Flierl, A. J. Morten, J. G. Richman, and J. F. Shriver, "Nonlinear cascades of surface oceanic geostrophic kinetic energy in the frequency domain," J. Phys. Oceanogr. **42**, 1577–1600 (2012).
[4] B. K. Arbic, M. Müller, J. G. Richman, J. F. Shriver, A. J. Morten, R. B. Scott, G. Serazin, and T. Penduff, "Geostrophic turbulence in the frequency-wavenumber domain: Eddy-driven low-frequency variability," J. Phys. Oceanogr. **44**, 2050–2069 (2014).
[5] A. N. Kolmogorov, "Dissipation of energy in locally isotropic turbulence," Dokl. Akad. Nauk SSSR **32**, 16 (1941).
[6] A. N. Kolmogorov, "The local structure of turbulence in incompressible viscous fluid for very large Reynolds' numbers," Dokl. Akad. Nauk SSSR **30**, 301–305 (1941).
[7] A. M. Obukhov, "On the distribution of energy in the spectrum of turbulent flow," Dokl. Akad. Nauk SSSR **32**, 22–24 (1941).
[8] A. M. Obukhov, "Spectral energy distribution in a turbulent flow," Izv. Akad. Nauk SSSR **5**, 453–466 (1941).
[9] L. Onsager, "The distribution of energy in turbulence," Phys. Rev. **68**, 286 (1945).
[10] R. H. Kraichnan, "Inertial ranges in two-dimensional turbulence," Phys. Fluids **10**, 1417–1423 (1967).
[11] R. H. Kraichnan, "Inertial-range transfer in 2-dimensional and 3-dimensional turbulence," J. Fluid Mech. **47**, 525–535 (1971).
[12] C. E. Leith, "Diffusion approximation for 2-dimensional turbulence," Phys. Fluids **11**, 671–672 (1968).
[13] G. K. Batchelor, "Computation of the energy spectrum in homogeneous two-dimensional turbulence," Phys. Fluids **12**, II-233–II-239 (1969).
[14] P. B. Rhines, "Waves and turbulence on a beta-plane," J. Fluid Mech. **69**, 417–443 (1975).
[15] S. Sukoriansky, N. Dikovskaya, and B. Galperin, "On the arrest of inverse energy cascade and the Rhines scale," J. Atmos. Sci. **64**, 3312–3327 (2007).
[16] G. K. Vallis and M. E. Maltrud, "Generation of mean flows and jets on a beta-plane and over topography," J. Phys. Oceanogr. **23**, 1346–1362 (1993).
[17] J. G. Charney, "The dynamics of long waves in a baroclinic westerly current," J. Meterol. **4**, 135–162 (1947).
[18] A. Hasegawa and K. Mima, "Pseudo-three-dimensional turbulence in magnetized nonuniform plasma," Phys. Fluids **21**, 87–92 (1978).
[19] N. Kukharkin and S. A. Orszag, "Generation and structure of Rossby vortices in rotating fluids," Phys. Rev. E **54**, R4524–R4527 (1996).
[20] A. Okuno and A. Masuda, "Effect of horizontal divergence on the geostrophic turbulence on a beta-plane: Suppression of the Rhines effect," Phys. Fluids **15**, 56–65 (2003).
[21] K. S. Smith, "A local model for planetary atmospheres forced by small-scale convection," J. Atmos. Sci. **61**, 1420–1433 (2004).
[22] Y. Zhang and Y. D. Afanasyev, "Beta-plane turbulence: Experiments with altimetry," Phys. Fluids **26**, 026602 (2014).
[23] D. L. Suhas and J. Sukhatme, "Low frequency modulation of jets in quasigeostrophic turbulence," Phys. Fluids **27**, 016601 (2015).
[24] C. Wortham, "A multi-dimensional spectral description of ocean variability with applications," Ph.D. thesis, Massachusetts Institute of Technology, 2013.
[25] B. K. Arbic and G. R. Flierl, "Baroclinically unstable geostrophic turbulence in the limits of strong and weak bottom Ekman friction: Application to midocean eddies," J. Phys. Oceanogr. **34**, 2257–2273 (2004).
[26] J. J. Early, R. M. Samelson, and D. B. Chelton, "The evolution and propagation of quasigeostrophic ocean eddies," J. Phys. Oceanogr. **41**, 1535–1555 (2011).
[27] P. Berloff and I. Kamenkovich, "On spectral analysis of mesoscale eddies. Part I: Linear analysis," J. Phys. Oceanogr. **43**, 2505–2527 (2013).
[28] P. Berloff and I. Kamenkovich, "On spectral analysis of mesoscale eddies. Part II: Nonlinear analysis," J. Phys. Oceanogr. **43**, 2528–2544 (2013).
[29] C. Canuto, M. Y. Hussaini, A. Quarteroni, and T. A. Zang, *Spectral Methods: Fundamentals in Single Domains*, Scientific Computation (Springer, Berlin Heidelberg, 2007).
[30] C. Canuto, M. Y. Hussaini, A. Quarteroni, and T. A. Zang, *Spectral Methods: Evolution to Complex Geometries and Applications to Fluid Dynamics*, Scientific Computation (Springer, Berlin Heidelberg, 2007).

[31] S. Sukoriansky, N. Dikovskaya, and B. Galperin, "Nonlinear waves in zonostrophic turbulence," Phys. Rev. Lett. **101**, 178501 (2008).

[32] B. Galperin, S. Sukoriansky, and N. Dikovskaya, "Geophysical flows with anisotropic turbulence and dispersive waves: Flows with a beta-effect," Ocean Dyn. **60**, 427–441 (2010).

[33] J. Theiss, "A generalized Rhines effect and storms on Jupiter," Geophys. Res. Lett. **33**, L08809, doi:10.1029/2005gl025379 (2006).

[34] A. B. Penny, A. P. Showman, and D. S. Choi, "Suppression of the Rhines effect and the location of vortices on Saturn," J. Geophys. Res. Planets **115**, E02001, doi:10.1029/2009JE003384 (2010).

[35] C. Eden, "Eddy length scales in the North Atlantic Ocean," J. Geophys. Res. Oceans **112**, C06004, doi:10.1029/2006JC003901 (2007).

[36] D. B. Chelton, M. G. Schlax, and R. M. Samelson, "Global observations of nonlinear mesoscale eddies," Prog. Oceanogr. **91**, 167–216 (2011).

[37] J. C. McWilliams and G. R. Flierl, "On the evolution of isolated, nonlinear vortices," J. Phys. Oceanogr. **9**, 1155–1182 (1979).

[38] M. E. Stern, "Minimal properties of planetary eddies," J. Mar. Res. **33**, 1–13 (1975).

[39] V. D. Larichev and G. M. Reznik, "2-dimensional solitary Rossby waves," Dokl. Akad. Nauk SSSR **231**, 1077–1079 (1976).

[40] G. R. Flierl, V. D. Larichev, J. C. McWilliams, and G. M. Reznik, "The dynamics of baroclinic and barotropic solitary eddies," Dyn. Atmos. Oceans **5**, 1–41 (1980).

[41] S. V. Antipov, M. V. Nezlin, V. K. Rodionov, E. N. Snezhkin, and A. S. Trubnikov, "Rossby solitons–stability, collisions, asymmetry and generation by flows with a velocity shear," Zh. Eksp. Teor. Fiz. **84**, 1357–1372 (1983).

[42] G. R. Flierl, "Isolated eddy models in geophysics," Annu. Rev. Fluid Mech. **19**, 493–530 (1987).

[43] G. R. Flierl, "On the instability of geostrophic vortices," J. Fluid Mech. **197**, 349–388 (1988).

[44] E. P. Chassignet and B. Cushman-Roisin, "On the influence of a lower layer on the propagation of nonlinear oceanic eddies," J. Phys. Oceanogr. **21**, 939–957 (1991).

[45] J. Nycander and G. G. Sutyrin, "Steadily translating anticyclones on the beta-plane," Dyn. Atmos. Oceans **16**, 473–498 (1992).

[46] S. G. L. Smith, "The motion of a non-isolated vortex on the beta-plane," J. Fluid Mech. **346**, 149–179 (1997).

[47] Z. Kizner, D. Berson, G. Reznik, and G. Sutyrin, "The theory of the beta-plane baroclinic topographic modons," Geophys. Astrophys. Fluid Dyn. **97**, 175–211 (2003).

[48] P. J. van Leeuwen, "The propagation mechanism of a vortex on the beta plane," J. Phys. Oceanogr. **37**, 2316–2330 (2007).

[49] G. M. Reznik, "Dynamics of localized vortices on the beta plane," Izv. Atmos. Oceanic Phys. **46**, 784–797 (2010).

[50] D. J. Benney, "Large-amplitude Rossby waves," Stud. Appl. Math. **60**, 1–10 (1979).

[51] S. P. Meacham and G. R. Flierl, "Finite-amplitude waves on barotropic shear layers and jets," Geophys. Astrophys. Fluid Dyn. **56**, 3–57 (1991).

[52] G. R. Flierl and A. R. Robinson, "On the time-dependent meandering of a thin jet," J. Phys. Oceanogr. **14**, 412–423 (1984).

[53] L. J. Pratt and M. E. Stern, "Dynamics of potential vorticity fronts and eddy detachment," J. Phys. Oceanogr. **16**, 1101–1120 (1986).

[54] L. J. Pratt, "Meandering and eddy detachment according to a simple (looking) path equation," J. Phys. Oceanogr. **18**, 1627–1640 (1988).

[55] B. Cushman-Roisin, L. Pratt, and E. Ralph, "A general theory for equivalent barotropic thin jets," J. Phys. Oceanogr. **23**, 91–103 (1993).

[56] J. Nycander, D. G. Dritschel, and G. G. Sutyrin, "The dynamics of long frontal waves in the shallow-water equations," Phys. Fluids A **5**, 1089–1091 (1993).

[57] L. M. Polvani, J. C. McWilliams, M. A. Spall, and R. Ford, "The coherent structures of shallow-water turbulence: Deformation-radius effects, cyclone/anticyclone asymmetry and gravity-wave generation," Chaos: Interdiscip. J. Nonlinear Sci. **4**, 177–186 (1994).

[58] R. M. Samelson, "Surface-intensified Rossby waves over rough topography," J. Mar. Res. **50**, 367–384 (1992).

[59] G. M. Reznik and T. B. Tsybaneva, "Planetary waves in a stratified ocean of variable depth. Part 1. Two-layer model," J. Fluid Mech. **388**, 115–145 (1999).

[60] A. V. Bobrovich and G. M. Reznik, "Planetary waves in a stratified ocean of variable depth. Part 2. Continuously stratified ocean," J. Fluid Mech. **388**, 147–169 (1999).

[61] A. Kubokawa, "Quasigeostrophic planetary waves in a two-layer ocean with one-dimensional periodic bottom topography," Geophys. Astrophys. Fluid Dyn. **102**, 119–137 (2008).

[62] N. W. McLachlan, *Theory and Application of Mathieu Functions* (Clarendon Press, 1947).

[63] E. Infeld, "Stability-criteria for generalized Mathieu equations," Q. Appl. Math. **34**, 301–304 (1976).

[64] L. Wille and P. Phariseau, "On the computation of a certain class of Hill determinants," J. Comput. Appl. Math. **15**, 83–91 (1986).

[65] F. M. Arscott, "The Whittaker-Hill equation and the wave equation in paraboloidal co-ordinates," Proc. R. Soc. Edinburgh Sect. A **67**(4), 265–276 (1967).

[66] K. M. Urwin and F. M. Arscott, "Theory of Whittaker Hill equation," Proc. R. Soc. Edinburgh Sect. A **69**, 28 (1970).

[67] F. W. Olver, D. W. Lozier, R. F. Boisvert, and C. W. Clark, *NIST Handbook of Mathematical Functions*, 1st ed. (Cambridge University Press, New York, 2010).

[68] K. M. Urwin, "Perturbation solutions of the Whittaker-Hill equation," IMA J. Appl. Math. **3**(2), 169-180 (1967).

[69] S. Danilov and D. Gurarie, "Scaling, spectra and zonal jets in beta-plane turbulence," Phys. Fluids **16**, 2592–2603 (2004).

[70] D. B. Chelton, R. A. DeSzoeke, M. G. Schlax, K. El Naggar, and N. Siwertz, "Geographical variability of the first baroclinic Rossby radius of deformation," J. Phys. Oceanogr. **28**, 433–460 (1998).

[71] D. Stammer, "Global characteristics of ocean variability estimated from regional TOPEX/POSEIDON altimeter measurements," J. Phys. Oceanogr. **27**, 1743–1769 (1997).

[72] A. Klocker, D. P. Marshall, S. R. Keating, and P. L. Read, "A regime diagram for ocean geostrophic turbulence," Q. J. R. Meteorol. Soc. **142**, 2411–2417 (2016).

[73] H. Nakano and H. Hasumi, "A series of zonal jets embedded in the broad zonal flows in the pacific obtained in eddy-permitting ocean general circulation models," J. Phys. Oceanogr. **35**, 474–488 (2005).

[74] T. Schneider and C. C. Walker, "Self-organization of atmospheric macroturbulence into critical states of weak nonlinear eddy-eddy interactions," J. Atmos. Sci. **63**, 1569–1586 (2006).

[75] N. A. Bakas and P. J. Ioannou, "A theory for the emergence of coherent structures in beta-plane turbulence," J. Fluid Mech. **740**, 312–341 (2014).

[76] A. P. Ingersoll, "Atmospheric dynamics of the outer planets," Science **248**, 308–315 (1990).

[77] B. Galperin, R. M. B. Young, S. Sukoriansky, N. Dikovskaya, P. L. Read, A. J. Lancaster, and D. Armstrong, "Cassini observations reveal a regime of zonostrophic macroturbulence on Jupiter," Icarus **229**, 295–320 (2014).

[78] R. K. Scott and D. G. Dritschel, "The structure of zonal jets in geostrophic turbulence," J. Fluid Mech. **711**, 576–598 (2012).

[79] R. K. Scott and A.-S. Tissier, "The generation of zonal jets by large-scale mixing," Phys. Fluids **24**, 126601 (2012).

[80] S. I. Thomson and M. E. McIntyre, "Jupiter's unearthly jets: A new turbulent model exhibiting statistical steadiness without large-scale dissipation," J. Atmos. Sci. **73**, 1119–1141 (2016).

[81] K. K. Tung, "On the onvergence of spectral series—A re-examination of the theory of wave propagation in distorted background flows," J. Atmos. Sci. **33**, 1816–1820 (1976).

[82] D. K. Lilly, "Numerical simulation of two-dimensional turbulence," Phys. Fluids **12**, II-240–II-249 (1969).

[83] M. E. Maltrud and G. K. Vallis, "Energy-spectra and coherent structures in forced 2-dimensional and beta-plane turbulence," J. Fluid Mech. **228**, 321–342 (1991).